

1 **Landers 1992 "reloaded": an integrative dynamic**
2 **earthquake rupture model**

3 Corresponding author: Stephanie Wollherr (wollherr@geophysik.uni-muenchen.de)

4 **Stephanie Wollherr¹, Alice-Agnes Gabriel¹, and P. Martin Mai²**

5 ¹Ludwig-Maximilians-University Munich

6 ²King Abdullah University of Science and Technology

7 **Key Points:**

- 8 • Physics-based simulation of the 1992 Landers earthquake including a new degree
9 of realism reproduces a broad range of observations
- 10 • Sustained dynamic rupture interconnecting the fault segments constraints pre-stress
11 and fault strength
- 12 • We discuss important implications of the observed interplay of fault geometry and
13 dynamic rupture transfers across the complex fault system

Corresponding author: Stephanie Wollherr, wollherr@geophysik.uni-muenchen.de

14 **Abstract**

15 The 1992 M_w 7.3 Landers earthquake is perhaps one of the best studied seismic events.
16 However, many aspects of the dynamics of the rupture process are still puzzling, e.g. how
17 did rupture transfer between fault segments? We present 3D spontaneous dynamic rup-
18 ture simulations of a new degree of realism, incorporating the interplay of fault geom-
19 etry, topography, 3D rheology, off-fault plasticity and viscoelastic attenuation. The sur-
20 prisingly unique scenario reproduces a broad range of observations, including final slip
21 distribution, seismic moment-rate function, seismic waveform characteristics and peak
22 ground velocities, as well as shallow slip deficits and mapped off-fault deformation pat-
23 terns. Sustained dynamic rupture of all fault segments in general, and rupture transfers
24 in particular, put strong constraints on amplitude and orientation of initial fault stresses
25 and friction. Source dynamics include dynamic triggering over large distances and di-
26 rect branching; rupture terminates spontaneously on most of the principal fault segments.
27 We achieve good agreement between synthetic and observed waveform characteristics and
28 associated peak ground velocities. Despite very complex rupture evolution, ground mo-
29 tion variability is close to what is commonly assumed in Ground Motion Prediction Equa-
30 tions. We examine the effects of variations in modeling parameterization, e.g. purely elas-
31 tic setups or models neglecting viscoelastic attenuation, in comparison to our preferred
32 model. Our integrative dynamic modeling approach demonstrates the potential of con-
33 sistent in-scale earthquake rupture simulations for augmenting earthquake source obser-
34 vations and improving the understanding of earthquake source physics of complex, seg-
35 mented fault systems.

1 Introduction

The M_w 7.3 Landers earthquake of June 28, 1992 ruptured five distinct segments previously considered unconnected. Overlapping fault zones of 80 km length hosted large vertical slips, large surface strike-slip offsets and unusual high stress-drops [*Kanamori et al.*, 1992; *Sieh et al.*, 1993]. Only two segments of the strike-slip fault system slipped over their respective total length, the previously unknown Kickapoo fault and the Homestead Valley fault (Fig. 1), while only parts of the other involved fault segments ruptured. The Landers event raised awareness of unexpectedly large magnitude earthquakes hosted by complicated fault networks; in particular the dynamic rupture transfer mechanisms which pose pressing questions of fault mechanics. Distinct ground shaking was recorded by a dense network of seismometers [*Campbell and Bozorgnia*, 1994] including locations very close to the slipping faults [*Chen*, 1995; *Sleep*, 2012].

The wealth of observational data has been analyzed to shed light on the slip distribution from inversion of seismological and geodetic data [e.g., *Wald and Heaton*, 1994; *Cohee and Beroza*, 1994; *Frey Mueller et al.*, 1994; *Cotton and Campillo*, 1995; *Fialko*, 2004a; *Xu et al.*, 2016] and to constrain rupture dynamics [e.g. *Peyrat et al.*, 2001; *Aochi and Fukuyama*, 2002; *Fliss et al.*, 2005; *Heinecke et al.*, 2014; *Wollherr et al.*, 2018]. Together with detailed analysis of the recorded strong ground motions [e.g., *Campbell and Bozorgnia*, 1994], rupture transfer mechanisms [e.g., *Wesnousky*, 2006; *Madden and Pollard*, 2012; *Madden et al.*, 2013] and potential energy release [e.g., *Dreger*, 1994; *Wald and Heaton*, 1994] a comprehensive picture of the source kinematics and macroscopic earthquake properties has been developed.

While the overall kinematics of the event are thought to be well understood, many observations regarding its complicated rupture dynamics are still unresolved. For instance, the Kickapoo-Landers fault unexpectedly connected the Johnson Valley fault and the Homestead Valley fault, which were previously assumed to be independent structures [*Sowers et al.*, 1994]. A well-recorded near-surface slip gap at the northern part of the Kickapoo fault, close to the junction to the Homestead Valley fault, suggests a disconnection between these faults. Thus, rupture is assumed to have propagated at depth and/or "jumped" via dynamic triggering to the adjacent fault segment [*Spotila and Sieh*, 1995]. Across the entire fault system, the rupture front is found to propagate at highly variable speeds [*Cotton and Campillo*, 1995; *Hernandez et al.*, 1999], slowing down at tran-

68 sitions between segments [*Wald and Heaton, 1994*] and in regions of high slip [*Cohee and*
69 *Beroza, 1994*].

70 The orientation of geometrically complex faults in the tectonic stress field has a
71 first-order impact on the mechanics of earthquakes and faulting [e.g., *Kaven and Pol-*
72 *lard, 2013*]. The Landers fault geometry is characterized by nearly vertical dip but ex-
73 hibits strike rotation by about 30° from its original direction of nucleation [*Bouchon and*
74 *Campillo, 1998*]. Of particular interest is the fact that the northern fault segments, in-
75 cluding the Emerson fault and Camp Rock fault, are not well oriented with respect to
76 the regional stress field, indicating locally higher fault strengths and lower initial shear
77 stresses. This leads to the hypothesis that large dynamic stress changes induced by rup-
78 ture of the adjacent fault segments are necessary to overcome static friction at the north-
79 ernmost faults [*Bouchon and Campillo, 1998*]. In contrast, the lack of aftershocks and
80 large fault offsets in conjunction with relatively shallow slip [*Wald and Heaton, 1994*],
81 suggests that the Camp Rock fault was rather statically triggered shortly after the event
82 [*Sieh, 1996; Kaneda and Rockwell, 2009*].

83 Physics-based dynamic rupture simulations allow investigating the full complex-
84 ity of the earthquake source dynamics by numerically modeling a spontaneously prop-
85 agating rupture on a prescribed fault surface. The space-time evolution of the rupture
86 is thereby governed by initial stresses on the fault, a frictional constitutive law, and the
87 bulk properties of the medium. *Olsen* [1997] presents the first dynamic rupture model
88 of the Landers event using a single planar fault and initial stresses derived from the slip
89 distribution of *Wald and Heaton* [1994]. Consequently, their model features very het-
90 erogeneous on-fault stress conditions. This model is then subsequently refined in an it-
91 erative dynamic rupture inversion approach [*Peyrat et al., 2001*] and well reproduces recorded
92 seismograms at selected sites for frequencies below 0.5 Hz.

93 However, simulations on single planar faults provide no insight on rupture trans-
94 fer between fault segments. Also, rupture nucleation, propagation and arrest are highly
95 sensitive to variations in fault geometry. Dynamically, rupture is able to overcome fault
96 bends, branch into or jump to adjacent fault segments only for specific fault pre-stresses,
97 limited distances between adjacent fault segments and limited branching angles of con-
98 nected faults [e.g., *Harris and Day, 1993; Bhat et al., 2007; Oglesby, 2008; Lozos et al.,*
99 *2011; DeDontney et al., 2012; Oglesby and Mai, 2012*].

100 Modeling complex fault geometries is challenging for numerical solvers, since the
101 detailed geometry must be honored explicitly by the spatial discretization. Numerical
102 schemes such as the Boundary Integral Equation Method (BIEM) [e.g., *Aochi and Fukuyama*,
103 2002; *Ando et al.*, 2017], Finite Element Methods (FEM) based on tetrahedral elements
104 [e.g., *Barall*, 2009] - including the Discontinuous Galerkin (DG) Method [e.g., *Pelties et al.*,
105 2012; *Tago et al.*, 2012] - or numerical methods using curvilinear elements [e.g., *Duru*
106 *and Dunham*, 2016] are able to accurately represent non-planar fault geometries. We point
107 out that the accurate representation of fault branches is restricted to methods that do
108 not use a traction-at-split nodes approach [*Andrews*, 1999; *Day et al.*, 2005; *Dalguer and*
109 *Day*, 2007], like BIEM and DG methods.

110 Only a few dynamic rupture scenarios considered the complex fault geometry on
111 which the Landers event occurred. A multi-segment geometry of the Landers fault zone
112 is first integrated into a dynamic rupture model by *Aochi and Fukuyama* [2002] and *Aochi*
113 *et al.* [2003]. By analyzing the effects of varying principal stress directions and frictional
114 parameters they conclude that rupture cannot propagate across all of the differently ori-
115 ented fault segments assuming a single principal stress orientation. That is, the local tec-
116 tonic setting and non-planar fault structure play the most significant role in this earth-
117 quakes generation and rupture process. However, the use of the BIEM restricted this study
118 to fully elastic, homogeneous material properties. Additionally, the Landers earthquake
119 serves as valuable validation and testing scenario, for example for demonstrating the ge-
120 ometrical flexibility of DG methods [*Tago et al.*, 2012; *Pelties et al.*, 2012; *Breuer et al.*,
121 2014]. However, these studies are not able to fully reproduce observations, as e.g. slip
122 on all fault segments or regional seismogram recordings. While these studies incorpo-
123 rate realistic fault geometries and topography, realistic material properties, such as 3D
124 subsurface structure and the possibility of plastic deformation, are missing.

125 In addition, significant fault-zone damage was observed for the Landers earthquake
126 [e.g., *Li et al.*, 1994a,b], motivating us to account for inelastic processes off the fault. Re-
127 cent advances in processing high-resolution aerial photographs of near-fault deformation
128 patterns reveal that off-fault deformation primarily correlates with fault complexity [*Milliner*
129 *et al.*, 2015]. A significant slip reduction towards the shallow part of the faults is inferred,
130 known as shallow slip deficit (SSD), which is often attributed to plastic deformation [*Fi-*
131 *alko*, 2004a; *Milliner et al.*, 2015; *Gombert et al.*, 2018]. Simulations on a non-planar yet
132 single fault plane reveal that purely elastic simulations underpredict the SSD [*Roten et al.*,

133 2017] as well as ground motions [Roten *et al.*, 2014, 2015]. Wollherr *et al.* [2018] includes
134 the full geometrical complexity of the fault system in scenario calculations demonstrat-
135 ing that spatio-temporal rupture transfers are significantly altered by off-fault plastic-
136 ity.

137 In this study, we develop an integrated dynamic source model for the the multi-
138 segment Landers earthquake based on physics-based HPC-enabled rupture simulations.
139 Our dynamic source model incorporates new degree of realism by integrating a compre-
140 hensive set of geological and geophysical information such as high-resolution topogra-
141 phy, rotating tectonic stresses, 3D velocity structure, depth-dependent bulk cohesion, and
142 a complex intersecting fault geometry. Unifying aforementioned complexities is enabled
143 by using SeisSol (www.seissol.org, Dumbser and Käser [2006]; Pelties *et al.* [2014]),
144 a software package specifically suited for handling complex geometries and for the effi-
145 cient use on modern high-performance computing infrastructure [e.g., Heinecke *et al.*,
146 2014; Uphoff *et al.*, 2017]. This work extends recent models presented in [Heinecke *et al.*,
147 2014; Wollherr *et al.*, 2018] which included complex fault geometries and off-fault plas-
148 ticity but were restricted to 1D velocity structure, constantly oriented tectonic background
149 stress and neglecting viscoelastic attenuation of the seismic wave field.

150 We find that the interplay of dynamic rupture transfers, geometric fault complex-
151 ity, spatially smoothly varying pre-stress, 3D velocity structure, topography, viscoelas-
152 tic attenuation and off-fault plasticity pose unique conditions for a mechanically self-consistent
153 dynamic source model. The such constrained simulation matches a broad range of re-
154 gional and local observations, including fault slip, seismic moment release and ground
155 motions. The presented model also contributes to the understanding of the shallow slip
156 deficit, directivity effects and rupture branching and "jumping" under realistic condi-
157 tions.

158 In the following, we first describe our modeling approach and the observational con-
159 straints considered. We then investigate the rupture characteristics of our preferred model
160 in terms of rupture branching, dynamic triggering, moment-rate release, and final slip
161 distribution in Sec. 3. We compare the ratio of shallow near-surface slip and deep slip
162 (within the seismogenic zone) to recent inversion results based on a Bayesian approach
163 [Gombert *et al.*, 2018], as well as the modeled off-fault plastic strain distribution with
164 near-field observations of fault zone width [Milliner *et al.*, 2015]. Analyzing ground mo-

165 tions in terms of spatial distribution and shaking levels (e.g. peak ground motions) with
166 respect to the observations proves an excellent quality of the synthetics produced by the
167 dynamic rupture model. We lastly discuss the effects of variations in modeling param-
168 eterization, e.g. purely elastic setups or models neglecting viscoelastic attenuation, in
169 comparison to our preferred model, as well as implications for understanding earthquake
170 dynamics on segmented fault systems in Sec. 4.

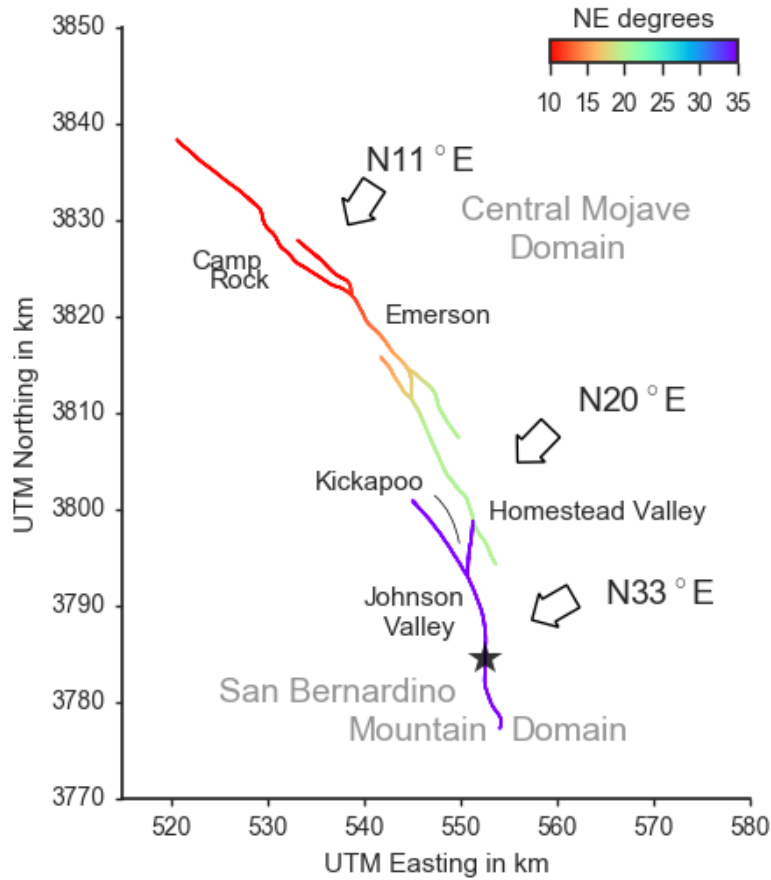


Figure 1: Mapped fault traces [Fleming *et al.*, 1998] and assumed orientation of maximum compressional principal stress σ_1 . The star marks the epicenter of the 1992 M_w 7.3 Landers earthquake.

171 **2 Model**

172 In the following, we describe our modeling approach and the observational constraints
 173 to construct a fully self-consistent dynamic rupture model of the 1992 Landers earth-
 174 quake. Dynamic rupture evolves spontaneously according to the parameterization of fric-
 175 tional behavior, initial fault stress state and nucleation conditions on prescribed fault
 176 surfaces. The nonlinear interaction of rupture propagation and the emanated seismic wave
 177 field is further affected by the structural characteristics, such as material properties and
 178 topography of the modeling domain.

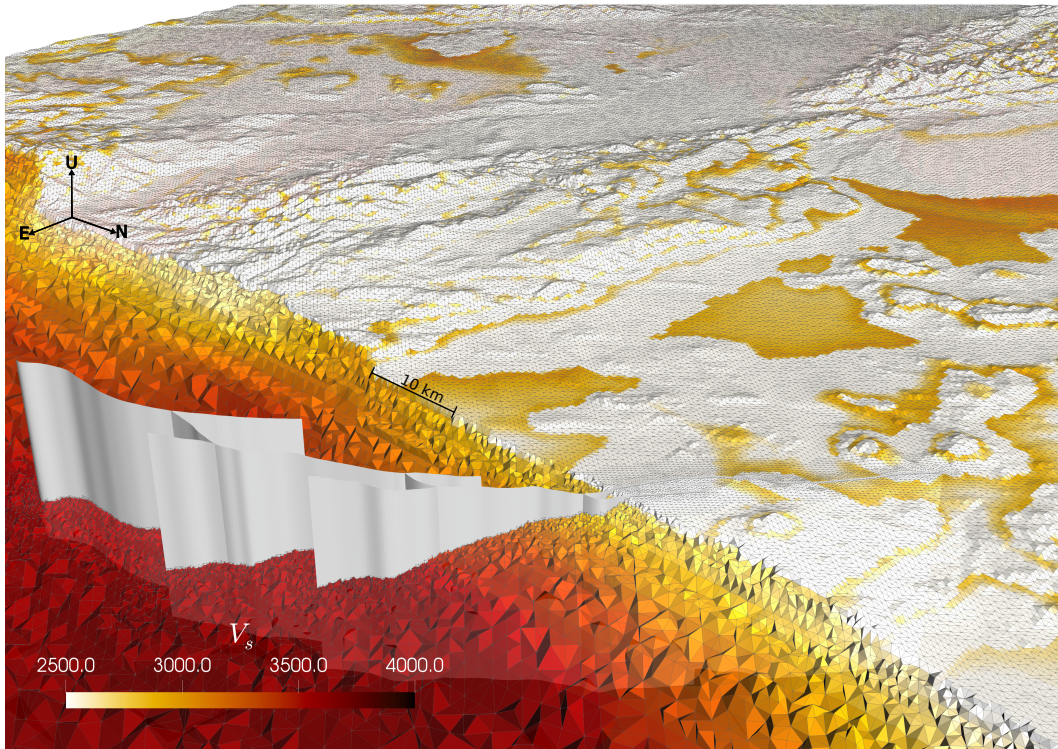


Figure 2: Structural model spatially discretized by tetrahedral computational elements. Colors represent the shear wave velocities V_s of the 3D velocity structure given by the Community Velocity Model-Harvard (CVM-H) [Shaw *et al.*, 2015]. Fault surface segments are visualized in white. Local refinement is applied in the vicinity of the faults (200 m) [Fleming *et al.*, 1998] and the Earth’s topography (500 m) [Farr *et al.*, 2007]. The fault surfaces intersect the local topography.

179

2.1 Structural Model and Numerical Discretization

180

181

182

183

184

185

186

187

The Landers fault system consists of curved, branched, and segmented faults. We construct the geometry of the main fault segments from photometric images of fault surface traces [Fleming *et al.*, 1998] that we extend to 15 km depth assuming purely vertical dip. The model includes five distinct non-planar fault segments connected over a total length of 80 km (see Fig. 1): the Johnson Valley fault (JVF) in the most southern part of the fault system, the Kickapoo fault (KF) connecting to the Homestead Valley fault (HVF), the Emerson fault (EF) including the connecting branch between the HVF and EF, and the Camp Rock fault (CRF) in the northernmost part. The fault sur-

188 face intersects the local topography, leading to fault elevation differences of up to 1000 m.
189 Our model incorporates DEM data of NASA’s Shuttle Radar Topography Mission (SRTM)
190 with 3-arc-seconds sampling (available from the U.S. Geological Survey [https://dds.
191 cr.usgs.gov/srtm/version2_1/SRTM3/](https://dds.cr.usgs.gov/srtm/version2_1/SRTM3/), ([Farr *et al.*, 2007])), re-sampled to match a
192 here chosen spatial topography discretization of 500 m. A cutout of the resultant struc-
193 tural model is visualized in Fig. 2.

194 In *Wollherr et al.* [2018] it was found, that the cohesive zone width may vary con-
195 siderably across geometrically complex fault systems, implying that a minimum intrin-
196 sic scale length needs to be resolved instead of some average. For our here preferred sce-
197 nario, we measure a minimum cohesive zone width of 155 m, located at the HVF at a
198 depth of 8 km. Following the convergence tests conducted in *Wollherr et al.* [2018], a
199 fault discretization of 200 m using polynomial basis functions of degree $p = 4$ or $\mathcal{O}5$
200 (corresponding to a minimum cohesive zone resolution of 0.78 m) sufficiently resolves the
201 cohesive zone width to ensure convergence defined by *Day et al.* [2005]. Due to the use
202 of sub-elemental Gaussian integration points, the fault is efficiently discretized by a max-
203 imum distance of 33.3 m (effective minimum cohesive zone width resolution of 4.65 points).
204 More details on the determination of the cohesive zone width and the required resolu-
205 tion are provided in the Appendix A: .

206 We define a high-resolution model area surrounding the fault traces over a width
207 and length of 270 km (east-west and north-south, respectively). Within this area, topog-
208 raphy is represented by tetrahedral elements with 500 m edge length (Fig. 2), further
209 refined by polynomial basis functions of degree $p = 4$ ($\mathcal{O}5$). Based on the locally re-
210 fined and high-order spatio-temporal discretization, we resolve a maximum of 1.0 Hz in
211 all analyzed synthetic waveforms in Sec. 3.5 within 105 km distance to the fault trace.
212 Synthetic measurements in the vicinity of low velocity basins resolve up to 1 Hz, while
213 high frequencies up to 4.0 Hz are resolved within 10 km distance to the fault trace, Fig.
214 B.1 in Appendix B: illustrates the model’s resolution exemplary for several stations with
215 varying distances to the fault trace ranging from 0.47 km (station LUC) to 102.8 km (sta-
216 tion SAL located on the Salton Sea Basin).

217 To avoid undesired reflections from the domain boundaries, while simultaneously
218 saving computational costs, we gradually increase the element size by a factor of 6% from

219 element to element up to an edge length of 10 km outside the high-resolution model area.
220 Equivalent mesh-coarsening is applied in the volume at depth.

221 **2.2 On-fault Initial Stresses**

222 We prescribe a smoothly varying principal stress field across our modeling domain,
223 without any small-scale or randomized heterogeneities. To this end, we combine infor-
224 mation on the regional tectonic setting, findings of previous dynamic rupture studies,
225 and newly conducted numerical experiments constraining the principal stress directions.

226 The state of stress governing the Landers main shock is only incompletely known
227 due to limited direct measurements of crustal stress in the Mojave block of the Eastern
228 California Shear Zone. The region is characterized by north-west trending strike-slip fault-
229 ing and a principal stress orientation of approximately N20°E [*Nur et al.*, 1989; *Hauks-*
230 *son*, 1994]. The Mojave block can be subdivided into several distinct domains based on
231 geometry and faulting style of tectonic activity [e.g., *Dokka and Travis*, 1990; *Unruh et al.*,
232 1994]. While the central and northern part of the fault system (i.e. HVF, EF and CRF)
233 belongs to the central Mojave block, *Unruh et al.* [1994] suggests that the JVF forms the
234 eastern boundary of a distinct domain around the San Bernardino Mountains charac-
235 terized by more north-striking strike slip faults.

236 To understand the details of the dynamic rupture process, the principal stress ori-
237 entations across the Landers fault system are particularly important. Focal-mechanism
238 analysis of the 1975 Galway and the 1979 Homestead Valley earthquakes, as well as of
239 background seismicity prior to the 1992 Landers main shock, yields a maximum prin-
240 cipal stress angle of 38° to 16° NE [*Hauksson*, 1994]. That is, the inferred principal stress
241 directions slightly rotate northwards up to the EF.

242 While background seismicity is mainly observed in the southern part of the fault
243 system, little is known about the stress state prior the Landers earthquake of the north-
244 ernmost segments [*Hauksson et al.*, 1993]. On the northern Landers fault system, an even
245 steeper oriented maximum principal stress might be plausible, given the locally consid-
246 erable higher maximum shear-strain orientation compared to the southern fault segments
247 [*Sauber et al.*, 1986]. *Aochi and Fukuyama* [2002] hypothesize a northern rotation to steep
248 angles based on the dynamically locked CRF in their simulations assuming a maximum
249 principal stress orientation of N22°E. A steep angle of 11° NE enabled full dynamic rup-

250 ture also of the northernmost segments under a non-rotating, depth-dependent background
251 stress [Heinecke et al., 2014; Wollherr et al., 2018].

252 In this study, we allow for smoothly varying directions of maximum principal stress,
253 consistent with regional stress estimates (summarized in Fig. 1). We assume that the
254 southern part of the fault system is contained in the San Bernardino Mountains domain
255 [Aochi and Fukuyama, 2002; Unruh et al., 1994], whereas all other fault segments are con-
256 sidered part of the central Mojave block. Therefore, in the south we prescribe a max-
257 imum principal stress orientation of N33°E governing the JVF and KF. The maximum
258 principal stress orientation changes to 20° between the KF and the HVF [Hauksson, 1994].
259 We then smoothly decrease the principal stress direction northwards from N20°E at the
260 HVF, consistent with the observed stress rotation postulated by Hauksson [1994].

261 Due to limited prior information, we perform several numerical experiments vary-
262 ing the principal stress orientation governing the CRF. We find that the CRF is orien-
263 tated very unfavorably under any angle between 15° and 38°. However, this segment rup-
264 tured with a substantial amount of slip [Kagan and Houston, 2005]. Sustained rupture
265 across the EF and CRF occurs in our model under a locally low angle of maximum prin-
266 cipal stress orientation of 11°, consistent with previous static and dynamic modeling stud-
267 ies of the full or southern-central fault system [Madden et al., 2013; Heinecke et al., 2014;
268 Wollherr et al., 2018].

269 While the prescribed stress field orientation is laterally smooth, the varying fault
270 strike orientation generates a heterogeneous initial stress state across all fault segments,
271 leading to both favorably and misaligned portions of the fault system. The Kickapoo branch
272 and the northern part of the HVF are the most favorably orientated segments. In con-
273 trast, the northernmost part of JVF, as well as the northernmost and southernmost parts
274 of the EF and CRF are not well aligned with respect to the regional principal stress ori-
275 entation. As a consequence, these fault segments experience only marginal or no slip (see
276 Sec. 3.2).

277 Principal stresses are assumed to vary linearly with depth, in accordance with rock
278 mechanics and field observations. Our prescribed intermediate principal stress compo-
279 nent, σ_2 , is purely vertical and set to the average confining pressure of the overlying rock
280 reduced by a constant hydrostatic pore fluid pressure [e.g., Suppe, 1985], i.e.

$$\sigma_2 = (2700 - 1000)\text{kg/m}^3 gz \quad (1)$$

281 with gravity $g = 9.8 \text{ m/s}^2$, average rock density of 2700 kg/m^3 , and depth z in m. We
 282 then determine the remaining two horizontal principal stress amplitudes using $\sigma_2 = (\sigma_1 +$
 283 $\sigma_3)/2$.

284 In addition, we apply the relative pre-stress ratio R [Aochi and Madariaga, 2003]
 285 to constrain the magnitude of the deviatoric stresses. Specifically, we strive to uniquely
 286 determine the horizontal principal stress amplitudes such that the stress field is most fa-
 287 vorably oriented at the hypocenter [Aochi and Madariaga, 2003], ensuring that the thus
 288 optimally oriented fault plane reaches failure before any other fault with different ori-
 289 entation.

290 For a given static and dynamic friction coefficient μ_s and μ_d , the R -ratio is defined
 291 as fault stress drop $\Delta\tau$ over breakdown strength drop $\Delta\tau_b$:

$$R = \frac{\Delta\tau}{\Delta\tau_b} = \frac{\tau^0 - \mu_d\sigma_n^0}{c + \mu_s\sigma_n^0 - \mu_d\sigma_n^0}. \quad (2)$$

292 Here, c denotes the frictional cohesion; τ^0 and σ_n^0 are the initial shear and normal stresses,
 293 respectively, at the hypocenter.

294 The relative level of initial stress has been found to determine rupture style and
 295 rupture properties [e.g., Gabriel *et al.*, 2012, 2013]. In our simulations, we assume $R =$
 296 0.65 which leads to a potential stress drop of 65% of the breakdown strength drop across
 297 the entire fault. Numerical experiments, testing R -ratios in the range of $0.5 < R <$
 298 0.9 , reveal that $R = 0.65$ optimally balances reasonable values of rupture speed and fi-
 299 nal slip while sustaining rupture across all fault segments by facilitating rupture trans-
 300 fers.

301 2.3 Frictional Properties

302 All frictional parameters are chosen constant across the fault system. Exceptions
 303 are the nucleation zone and the northernmost part of the fault system, where we account
 304 for palaeoseismological evidence. We further assume a smooth fault strength increase
 305 with depth.

306 Based on laboratory experiments [e.g., Ida, 1972] we use linear slip-weakening fric-
 307 tion. We choose a static friction coefficient $\mu_s = 0.55$ close to Byerlee's coefficient which
 308 is consistent with regional stress inversions [Gross and Kisslinger, 1997]. Under linear
 309 slip-weakening friction, a high stress drop is required to facilitate rupture transition be-

310 tween distinct fault segments. Correspondingly, we find a dynamic coefficient of friction
311 of $\mu_d = 0.22$ to optimally facilitate rupture cascading. Frictional cohesion is set to 2 MPa
312 for the entire fault system. The resulting average stress drop over all positive slip regions
313 is approximately 12.5 MPa with a maximum stress drop of 33 MPa at 8 km depth. Sur-
314 prisingly high stress drops were found for the Landers earthquake from energy to mo-
315 ment rate ratios [Kanamori *et al.*, 1992; Sieh *et al.*, 1993] and also agree with what is
316 inferred from kinematic stress inversion [Bouchon and Campillo, 1998].

317 We observe a strong trade-off between rupture speed and critical slip distance D_c
318 denoting the amount of slip over which friction drops from μ_s to μ_d . The critical slip dis-
319 tance also crucially affects rupture transitions by determining a critical nucleation size
320 required to initiate spontaneous rupture via dynamic triggering. In numerical experiments
321 we find that $D_c = 0.62$ m ensures a balance of efficient rupture transfer between adja-
322 cent faults (in accordance with the moment rate release) and the prevention of pronounced
323 supershear rupture.

324 While previous dynamic rupture simulations of the Landers earthquake choose D_c
325 in the range of 0.8 m [Olsen, 1997; Peyrat *et al.*, 2001], we find that lower D_c is required
326 to sustain rupture across the here geometrically more complex fault system. Besides ge-
327 ometric effects, a lower D_c can be attributed to the effect of off-fault plasticity [Roten
328 *et al.*, 2017; Wollherr *et al.*, 2018].

329 Paleoseismological evidences point to a large event occurring at the EF and CRF
330 approximately 2000–3000 years ago, while the southern part of the fault system has not
331 failed for 8000–9000 years [Sieh, 1996]. This suggests locally lower fault strengths due
332 to not yet recovered static friction or lower regional stresses due to the more recent stress
333 release. While we choose a constant stress ratio across the entire fault zone, we locally
334 decrease fault strength by choosing $\mu_s = 0.44$ instead of 0.55 at the EF and the CRF
335 segments. Our simulations reveal that such a only slightly weaker CRF and EF are cru-
336 cial to facilitate dynamically triggered initiation of rupture on these segments.

337 Rupture is initiated using a artificial nucleation procedure within a circular patch
338 of a 1.5 km radius. Within this zone, the friction coefficient is gradually reduced from
339 its static to its dynamic value over a specified time of 0.5 s [Bizzarri, 2010]. Outside this
340 zone, forced rupture is smoothly overtaken by spontaneous rupture. The hypocentral depth

341 is set to 7 km as constrained by source inversion [*Wald and Heaton, 1994; Cotton and*
342 *Campillo, 1995; Hernandez et al., 1999*].

343 At depth, we account for the transition from the brittle to ductile regime between
344 -9 km to -15 km. We linearly increase dynamic friction gradually up to static friction
345 values which allows rupture to stop smoothly. By increasing fault strength instead of pre-
346 stress with depth we ensure off- and on-fault stresses are equal which is necessary when
347 accounting for off-fault plasticity.

348 **2.4 Bulk Properties and Plasticity**

349 Our model incorporates the 3D velocity structure of the Community Velocity Model-
350 Harvard (CVM-H, version 15.1.0, *Shaw et al. [2015]*), exemplarily visualized for a cutout
351 in Fig. 2. Velocity and density information are efficiently mapped onto the parallelized
352 computational mesh using the geoinformation server ASAGI [*Rettenberger et al., 2016*].
353 The lowest shear-wave velocities of the domain and across the fault determine the wave
354 field resolution reached in the simulation. Shear-wave velocities range from 4500 m/s to
355 320 m/s in the sedimentary basin around the Salton sea. At the fault, shear-wave ve-
356 locities are 2800 m/s at shallow depths, and do not exceed 3500 m/s at the bottom of
357 the fault, determining the upper bound for subshear rupture speeds. Besides the low-
358 velocity basins at the Salton sea and at the San Bernardino basin (minimum wave speed
359 of 680 m/s) the lowest wave speeds within the high resolution model domain is 900 m/s.
360 The simulation employs viscoelastic rheologies to model intrinsic attenuation [*Uphoff and*
361 *Bader, 2016*]. We couple Q to the velocity model by using $Q_s = 50.0v_s$ and $Q_p = 2Q_s$
362 following commonly used parametrization [*Graves et al., 2008*]. We discuss the effect of
363 attenuation on dynamically triggered rupture in detail in Sec. 4.4.

364 Additionally, our model makes use of a computationally efficient implementation
365 of Drucker-Prager off-fault plasticity within SeisSol [*Wollherr et al., 2018*]. To this end,
366 a domain-wide initialization of initial stresses and bulk cohesion and friction is required,
367 which we base on regional observations from the Landers fault zone area. Here, equiv-
368 alent initial on- and off-fault stresses are assumed, accounting for the smooth principal
369 stress rotation between the San Bernardino Mountain Domain and the Central Mojave
370 block.

371 Furthermore, the formulation of the plastic yield criterion requires the specifica-
372 tion of bulk cohesion. Cohesion differs for different rock types, and also depends on depth
373 and the respective damage level of the host rock. In the Landers region, the main near-
374 surface rock type is granodiorite [Dibblee, 1967]. Correspondingly, we assume a relatively
375 undamaged granite-type rock, described as "good quality rock" in *Roten et al.* [2017])
376 who use a Hoek-Brown model to constrain cohesion values for a given rock type and dam-
377 age level. We therefore define a depth-dependent parametrization of cohesion, ranging
378 from $c = 2.5$ MPa at the surface to $c = 30$ MPa at 6 km depth and $c = 50$ MPa at 14 km
379 depth. While cohesion depends on depth, bulk friction is assumed constant in the en-
380 tire model domain. We set bulk friction everywhere as equal to 0.55, resembling static
381 friction of most fault segments. While the static friction coefficient of the northern seg-
382 ments is reduced (see previous section), we assume that off-fault rock properties are not
383 considerably altered by paleoseismological events.

384 In case of plastic yielding, plastic strain at time t can be mapped into the scalar
385 quantity $\eta(t)$ (e.g., visualized in Fig. 11) following *Ma* [2008]:

$$\eta(t) = \int_0^t d\eta = \int_0^t \sqrt{\frac{1}{2} \dot{\epsilon}_{ij}^p \dot{\epsilon}_{ij}^p}. \quad (3)$$

386 with $\dot{\epsilon}_{ij}^p$ being the inelastic strain rate.

387 2.5 Numerical Method

388 We use the open-source software package SeisSol (www.seissol.org; freely available
389 at github.com/SeisSol/SeisSol) to conduct large-scale dynamic rupture simulations of
390 the 1992 Landers earthquake unifying all modeling ingredients described above. SeisSol
391 is based on an Arbitrary high order DERivative-Discontinuous Galerkin (ADER-DG)
392 approach which enables high-order accuracy in space and time [*Käser and Dumbser*, 2006;
393 *Dumbser and Käser*, 2006]. The software solves the non-linear problem of spontaneous
394 frictional failure on prescribed fault surfaces coupled to seismic wave propagation [*De la*
395 *Puente et al.*, 2009; *Pelties et al.*, 2012]. It allows to precisely model seismic waves trav-
396 eling over large distances in terms of propagated wavelengths with minimal dispersion
397 errors [*Käser et al.*, 2008] and features fully adaptive, unstructured tetrahedral grids that
398 allow for complicated geometries and for rapid mesh generation [*Wenk et al.*, 2013].

399 The software is verified in community benchmarks addressing a wide range of dy-
400 namic rupture problems including: branched and curved faults, dipping faults, labora-

401 tory derived friction laws, and on-fault heterogeneities. [*Pelties et al.*, 2014; *Harris et al.*,
402 2018]. End-to-end optimization [*Breuer et al.*, 2014; *Heinecke et al.*, 2014; *Breuer et al.*,
403 2015, 2016; *Rettenberger and Bader*, 2015; *Rettenberger et al.*, 2016] targeting high ef-
404 ficiency on high-performance computing infrastructure includes a ten-fold speedup by
405 an efficient local time-stepping algorithm [*Uphoff et al.*, 2017]. Viscoelastic rheologies
406 are incorporated using an offline code-generator to compute matrix products in a com-
407 putationally highly efficient way. This poses an increase in computational cost of a fac-
408 tor of only 1.8 in comparison to a purely elastic model (of $\mathcal{O}6$) while resolving the full
409 memory variables [*Uphoff and Bader*, 2016]. Similarly, the off-line code generator is used
410 for incorporating off-fault plasticity within a nodal basis approach [*Wollherr et al.*, 2018].
411 The computational overhead of off-fault plasticity falls in the range of 4.5% – 13.1% de-
412 pendent on the number of elements that yield plastically and the polynomial degree of
413 the basis functions. This relatively minor increase of costs enables the use of realistic ma-
414 terial properties for large-scale scenarios - and we demonstrate the considerable affects
415 of both, viscoelastic attenuation and off-fault plastic yielding on rupture dynamics and
416 ground motion synthetics in Sec. 4.

417 The structural model created with GoCad [*Emerson Paradigm Holding*, 2018] is
418 discretized using the meshing software Simmetrix by Simmodeler [*Simmetrix Inc.*, 2017]
419 to generate a mesh consisting of 20 million elements. For all presented simulations we
420 use a spatio-temporal discretization of polynomial degree $p=4$ ($\mathcal{O}5$). The models account-
421 ing for off-fault plasticity and attenuation run for 6:53 h on 525 nodes on supermuc phase
422 1. Note, that the computational costs are higher in comparison to previously presented
423 scenarios [*Wollherr et al.*, 2018] for a similar mesh size due to the additional costs of vis-
424 coelastic damping and a higher polynomial degree.

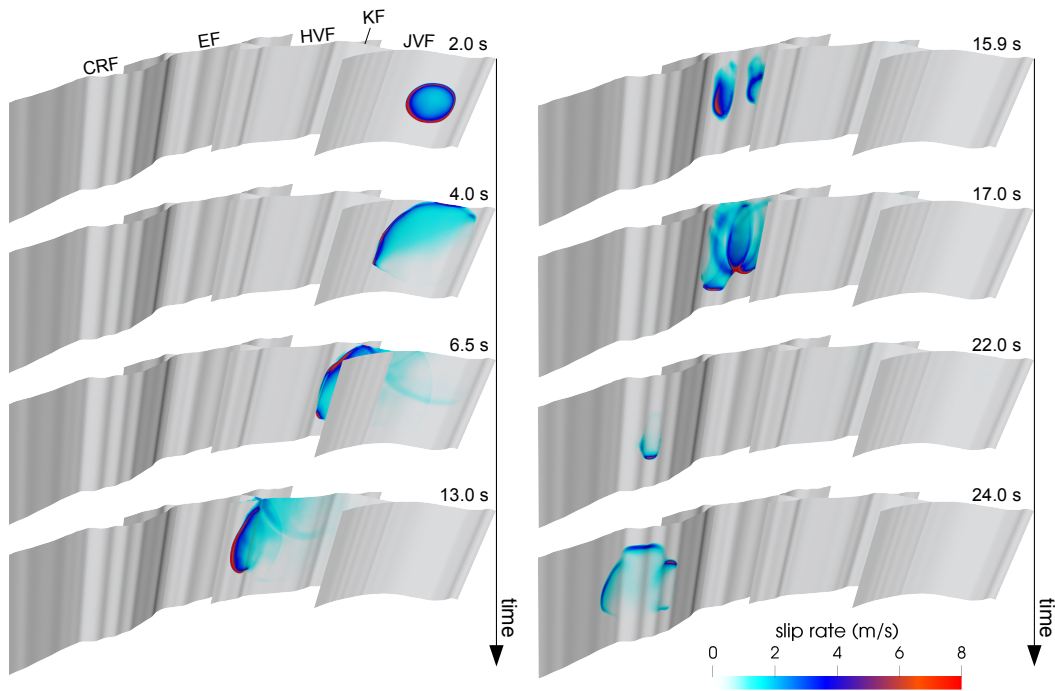


Figure 3: Slip rate across the fault system at selected rupture times illustrating dynamic rupture evolution and complexity. Rupture successively cascades by direct branching and dynamic triggering.

425 3 Results

426 In the following, we present a fully 3D dynamic rupture model combining complex
 427 fault geometries and off-fault plastic yielding with realistic rheology, viscoelastic atten-
 428 uation and 3D subsurface structure. Our preferred model reproduces a broad range of
 429 regional (moment release, waveforms and peak ground velocities) and near-fault (slip dis-
 430 tribution, shallow slip deficit, fault zone damage) observations. The model captures dy-
 431 namic rupture transfers between fault segments and furthers our understanding of the
 432 activation of fault branches and the potential for dynamic triggering of adjacent fault
 433 segments.

3.1 Rupture Dynamics

In our dynamic model rupture propagates spontaneously across five fault segments. Rupture successively cascades by direct branching and dynamic triggering. The evolution of slip-rate across the fault segments at selected time steps is visualized in Fig. 3. A high-resolution animation is provided in the supporting information (S1).

Our simulation features very complex rupture propagation patterns. In particular: i) we observe a variety of rupture transfer mechanisms between fault segments: direct branching, jumping by dynamic triggering, or combination of both, in forward and reverse direction; ii) we find that dynamically triggered rupture transfer is crucial to enable sustained rupture across the entire fault system; iii) multiple rupture fronts exist at certain times that may propagate in opposite directions, and iv) rupture speed is highly variable in correlation with the fault geometry, its orientation with respect to the pre-stress and rupture transfers.

In the following we describe in detail the source dynamics in terms of rupture propagation through the complex fault system. Rupture smoothly nucleates within the first 0.6 s and then spontaneously propagates across the southern part of the Johnson Valley fault segment (JVF). At the fault intersection with the Kickapoo fault (KF), we observe complete rupture transfer by direct branching at high rupture speed at 4 s.

After completely rupturing the KF, slip on the Homestead Valley Fault (HVF) is initiated. However, the pronounced fault bend at the fault intersection nearly stops rupture after approximately 6.5 s rupture time creating localized small slip patches at shallow depths at its northern part. After a delay of almost 1 s, rupture re-initiates at a depth of 7–8 km and continues breaking across the full northern extend of the HVF.

At around 11.9 s, rupture is delayed upon branching into the small fault segment connecting the HVF and the Emerson fault (EF). In distinction to the Kickapoo branching, rupture here also continues along its original branch until it is stopped by the boundary of the HVF segment. The EF is first activated at shallow depth by dynamic triggering from waves originating directly from the HVF which eventually dies out. Rupture is activated for a second time just a few seconds later at depth of 6 km, while a slower propagating rupture front arrives after direct branching via the connecting segment. As a consequence, we observe multiple rupture fronts and reversely (towards the south) prop-

465 agating rupture, as well as repeated slip of the KF. Parts of the HVF and the KF are
466 dynamically re-activated due to the backward propagating rupture when multiple rup-
467 ture fronts at the EF meet.

468 Finally, at 22.3 s rupture time, the CRF is dynamically activated at a depth of 8 km
469 by the superimposed wave field of the subsequent failure of the northern part of the HVF
470 (9 km from the triggered part of the CRF) and the EF (16 km from the triggered part
471 at the CRF). Rupture propagates with a strong up-dip component across the central part
472 of the CRF, and then dies out shortly after reaching the surface. Fault slip completely
473 arrests after 30 s of rupture time.

474 Our high-resolution model allows to clearly distinguish between rupture branch-
475 ing and rupture (re-)nucleation by dynamic triggering. Rupture chooses to continue along
476 secondary fault segments (branches) whenever these are more favorably orientated than
477 the main fault segment. We observe rupture branching twice: between the JVF, KF and
478 HVF and between the HVF and the EF. In the first case, the optimal orientation of KF
479 towards the background stress field favors rupture propagation. Thus, rupture completely
480 stops at the JVF and rather follows the KF branch. For the second branching transfer
481 (between the HVF and EF), the connecting branch is less favorably oriented. Rupture
482 only partially follows the branch while also continuing along the originating fault seg-
483 ment (HVF).

484 Dynamic stresses propagate like seismic waves from rupturing fault segments to-
485 wards locked parts of the fault system, eventually nucleating rupture without requiring
486 the direct arrival of a rupture front. Note that the main rupture front is unable to over-
487 come the geometrical barrier between the EF and the CRF. However, unlike previous
488 dynamic rupture scenarios, our model succeeds in rupturing the CRF by dynamic trig-
489 gering. This is facilitated by a steep angle of principal stress direction governing the north-
490 ern fault system, a reduced fault strength, and in particular the emitted seismic waves
491 from the almost simultaneous failure of the northern part of the HVF and the EF. The
492 stress changes due to failure of both fault segments are high enough to trigger fault slip
493 over a distance of 9 km (from the EF) and 15 km (from the HVF). The abrupt decel-
494 eration of rupture in between the KF and HVF additionally triggers small patches of shal-
495 low slip at the HVF, but also at the most southern part of the EF, which eventually die
496 out (at around 7.9-9.5s).

497 Rupture speed v_r is highly variable across the fault system. On average, we find
498 $v_r \approx 2300$ m/s consistent with earlier studies [*Wald and Heaton, 1994; Hernandez et al.,*
499 *1999*]. Rupture accelerates and decelerates in relation to changes of fault orientation and
500 rupture transfers to adjacent segments. We observe very slow local rupture speeds at ge-
501 ometrical barriers, such as $v_r = 1200$ m/s at the transition from the KF to the HVF,
502 and again when rupture reaches the EF.

503 Supershear transitions are rarely observed in nature, but due to the low resolution
504 of the data it remains still unclear if small supershear patches can occur locally. Small
505 patches of supershear rupture are locally induced in our model at shallow depths. Specif-
506 ically, we observe supershear due to the interaction of the rupture front with the free sur-
507 face at the KF and at the HVF, as in previous dynamic rupture models [*Olsen, 1997;*
508 *Peyrat et al., 2001*]. Additionally, branching triggers local supershear episodes (cf. the
509 JVF-KF branching at approximately 5.6 s rupture time).

510 Rupture termination, and the potential resultant generation of stopping phases,
511 is of specific interest when analyzing rupture in complex, multi-segment fault systems
512 [*Oglesby, 2008*]. From a geological point of view, it was a surprising observation to find
513 that the northern part of the Johnson Valley fault did not slip [e.g. *Rockwell et al., 2000*].
514 Our dynamic rupture model provides a consistent explanation for spontaneous rupture
515 termination on most of the principal fault segments, although fault structures in real-
516 ity continue.

517 Rupture termination in our model is overall independent of the prescribed geomet-
518 ric fault endings, except for the northernmost section of the HVF. In all other cases, rup-
519 ture is spontaneously stopped due to local fault geometry in conjuncture with the local
520 principal stress orientation: First, rupture is smoothly stopped at the first fault segment
521 in backward direction by the change of fault orientation at the most southern part of the
522 JVF. Second, rupture completely follows the Kickapoo branch, not rupturing the north-
523 ern part of the JVF. Additionally, rupture only initiates in the central part of the CRF
524 and smoothly dies out towards the southern and northern part of the fault. These re-
525 sults are consistent with the rupture termination analysis by *Sieh [1996]* (their Fig. 8
526).

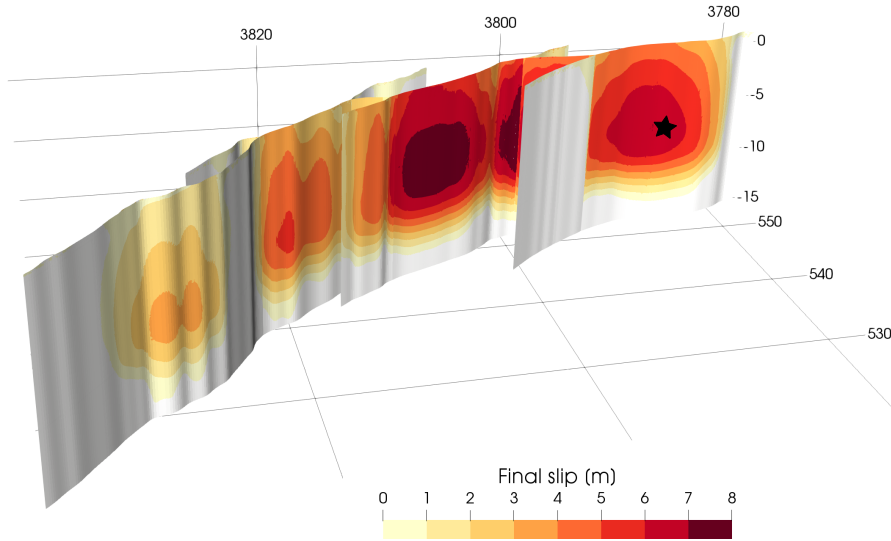


Figure 4: Distribution of total accumulated slip for the preferred dynamic rupture scenario after 100 s simulation time. Coordinate axis are in UTM coordinates (km). The star marks the hypocenter at depth of -7 km.

527

3.2 Slip Distribution

528

529

530

531

532

533

534

Numerous studies estimated the on-fault slip distribution of the Landers earthquake [e.g., *Campillo and Archuleta*, 1993; *Wald and Heaton*, 1994; *Cohee and Beroza*, 1994; *Cotton and Campillo*, 1995; *Fialko*, 2004a; *Milliner et al.*, 2015; *Gombert et al.*, 2018]. While these studies are based on different source inversion approaches and datasets, they overall agree that the largest slip is encountered on the HVF. However, the inferred slip distributions also reveal a large degree of non-uniqueness owing to inherent difficulties in finite-fault slip inversion and the resulting variations in slip models [*Mai et al.*, 2016].

535

536

537

538

539

The accumulated slip of our simulation is visualized in Fig. 4. Fault slip is distributed over the southern part of the JVF, the KF, the central and northern part of the HVF, the central EF, and the central part of the CRF. Slip below 1-2 m is observed at the southern HVF, and also at the most southern and northern part of the EF where rupture is triggered dynamically. The northern part of the JVF is not ruptured in our simulation.

540

541

For all fault segments, slip at depth (5-10 km) is always larger than at shallow depths (less than 5 km). Slip peaks at 7 m located at 5.5 km depth of the central HVF in the

542 vicinity to the KF branching point. At this location, the fault abruptly changes its ori-
543 entation, forming a geometrical barrier that decelerates the rupture while simultaneously
544 accumulating slip.

545 In the northern part of the fault system we observe an apparent discrepancy of mod-
546 eled co-seismic slip with observations. Near-surface slip on the CRF does not exceed 0.5 m
547 in our simulation, while slip at depth reaches up to 4 m. In contrast, the imaged CRF
548 slip values are high at shallow depth [*Sieh et al.*, 1993; *Wald and Heaton*, 1994]. How-
549 ever, *Sieh* [1996] and *Kaneda and Rockwell* [2009] suggest that the CRF might have slipped
550 as a consequence of static stress changes shortly after the main event. We discuss this
551 hypothesis with respect to our simulation results in Sec. 4.5.

552 3.3 Seismic Moment Rate

553 The Landers earthquake was the largest earthquake to strike the contiguous United
554 States in 40 years. The event’s total seismic moment has been inferred between $6.0\text{e}+19$ –
555 $16.0\text{e}+19$ Nm (moment magnitude M_w 7.15–7.4) [*Kanamori et al.*, 1992; *Campillo and*
556 *Archuleta*, 1993; *Sieh et al.*, 1993; *Wald and Heaton*, 1994; *Dreger*, 1994; *Cohee and Beroza*,
557 1994; *Vallée and Douet*, 2016]. The seismic moment of our dynamic rupture scenario is
558 with $M_0 = 11.2\text{e}+19$ Nm (M_w 7.29), in excellent agreement with previous estimates from
559 kinematic models and geological studies.

560 The multi-segment character of the event reflects on the moment release over time.
561 Most previous studies divide it into two major subevents [*Campillo and Archuleta*, 1993;
562 *Dreger*, 1994; *Cohee and Beroza*, 1994], postulating that slip on the JVF and KF released
563 approximately 20-25% of the total seismic moment, while the northern part of the fault
564 system, including the JVF, the EF and CRF, released approximately 75-80%.

565 Fig. 5 compares the moment-release rate from our dynamic rupture simulation to
566 three observationally inferred moment-rate functions. The optimal and average seismic
567 moment rate of the SCARDEC database are retrieved from teleseismic body waves (*Vallée*
568 *and Douet* [2016], gray dotted and black solid lines in Fig. 5). The source time function
569 inferred from the surface slip distribution (*Kagan and Houston* [2005], blue in Fig. 5)
570 is based on the assumption that slip to a depth of 5 km equals to $\approx 69\%$ of the surface
571 slip. Note that we use our simulation as reference time, and shift the moment rate re-
572 lease of the SCARDEC solution by 5 s to match the main moment rate peaks.

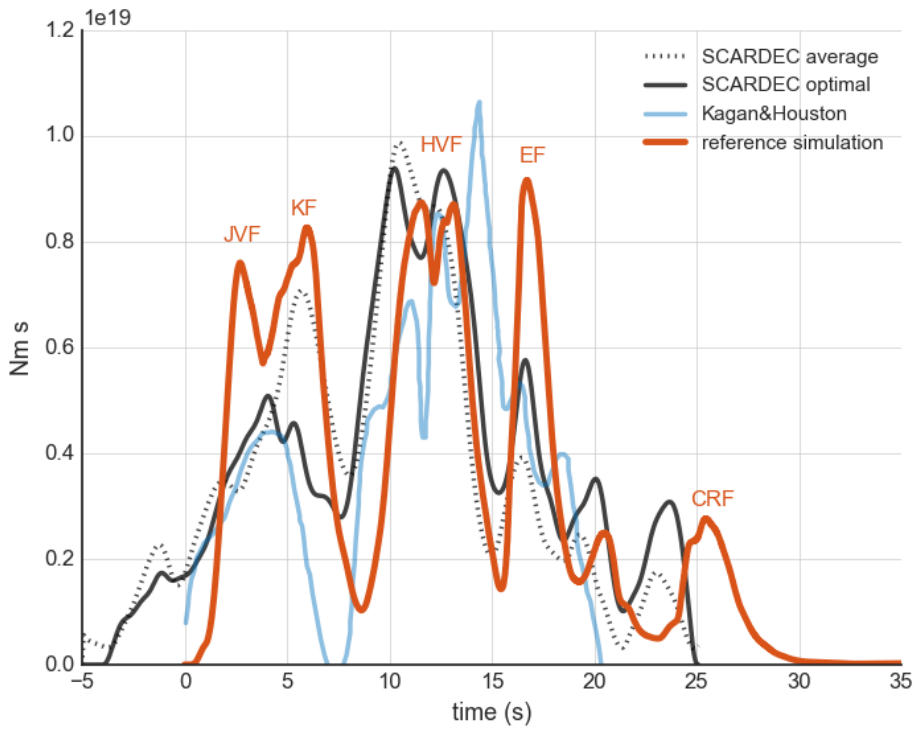


Figure 5: Seismic moment-release rate over time. Dynamic rupture simulation (orange) compared to the optimal and average moment rate of the SCARDEC database (in black and dotted light gray, *Vallée and Douet* [2016]) and moment rate based on the surface slip (in light blue, *Kagan and Houston* [2005]). The time line is taken from our simulation, the SCARDEC solutions are shifted by -5 s accordingly to match the main moment rate peaks.

573 The seismic moment rate of our simulation well reproduces the major moment-rate
574 peaks of the SCARDEC solution. The first is associated with rupture of the JVF and
575 KF within the first 7 s. The next peak between 7 s and 15 s corresponds to the failure
576 of the HVF releasing the largest individual contribution to overall seismic moment. Sub-
577 sequently, we reproduce several distinct local peaks after 15 s that we associate with the
578 cascading rupture of the individual northernmost fault segments (e.g. the EF and CRF).

579 Pronounced delays of moment-release rate in observations as well as our simula-
580 tion may be correlated with rupture transferring between fault segments. Specifically,
581 dynamic triggering (rupture jumping) has been associated with the observed segmen-
582 tation of moment release. However, our dynamic rupture model reveals that dynamic
583 triggering is not the only factor reducing the moment release significantly. Specifically,
584 rupture deceleration due to fault geometry strongly affects the moment release, thus com-
585 plicating the inference of rupture transfers from observations.

586 Rupture propagation along the HVF (at ≈ 7 s) is delayed by ≈ 0.5 -1.0 s, in the SCARDEC
587 solutions as well as our simulation result. The moment rate provided by *Kagan and Hous-*
588 *ton* [2005] even accounts for a delay of 2.0-2.5 s and a complete stop of moment release,
589 which may correspond to the observed slip gap near the surface [*Spotila and Sieh*, 1995].
590 Previous studies interpret this delay of rupture propagation as an indication of rupture
591 jumping from the KF to the HVF[e.g., *Campillo and Archuleta*, 1993]. However, our sim-
592 ulation suggests that this delay rather corresponds to a slow rupture propagation after
593 the branching between the KF and the HVF. Rupture encounters a pronounced fault bend
594 at the center of the HVF and is dynamically slowed down. Rupture re-initiating is then
595 potentially facilitated by arriving seismic waves from the failure of previous segments as
596 discussed in Sec. 4.4.

597 The most prominent differences in the moment rate functions are found in the early
598 rupture stage. In addition, our scenario overestimates the moment release at 17 s (rup-
599 ture of the EF) with respect to the SCARDEC solution. However, this high moment rate
600 release at the EF could be related to the highest peak of the moment rate of *Kagan and*
601 *Houston* [2005] at 14 s. On the other hand, peak moment rates are underestimated around
602 10 and 15 s (rupture of the HVF and the connecting branch between the HVF and EF).
603 We further discuss these discrepancies in dependence of the model assumptions and ar-
604 tificial nucleation procedure in Sec. 4.1.

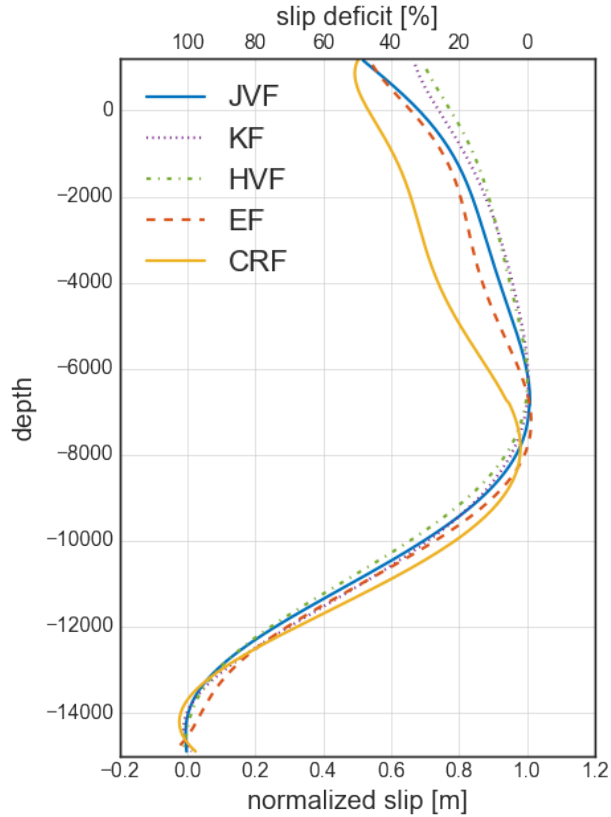


Figure 6: Normalized slip (bottom axis) and corresponding shallow slip deficit (top axis) for each fault segment in dependence of fault depth for our preferred Landers earthquake simulation. Each line represents the average over the corresponding fault segment.

605 3.4 The Shallow Slip Deficit and Stress Drop

606 In this section we investigate the shallow slip deficit (SSD) - the reduction of shal-
 607 low slip relative to slip at depth - in our simulation. The SSD is frequently observed in
 608 geodetic slip inversions for major strike-slip earthquakes, including the 1992 Landers event
 609 [e.g., *Fialko, 2004a; Milliner et al., 2015*]. We show that an along-strike variability of the
 610 SSD is possible, even for laterally constant rock cohesion and bulk friction.

611 The SSD of the Landers earthquake is estimated to be of the order of 30-60% [e.g.,
 612 *Cohee and Beroza, 1994; Fialko, 2004a; Milliner et al., 2015*]. Recent coseismic slip mod-
 613 els derived by a Bayesian approach suggest that the overall SSD for the Landers event
 614 is about 40%, but might vary between fault segments [*Gombert et al., 2018*].

615 The origin of the SSD is still under debate. While *Xu et al.* [2016] argue that the
616 majority of inferred SSD is a result of poor resolution of near-fault surface data in slip
617 inversions, it is often attributed to coseismically occurring plastic deformation at shal-
618 low depths [e.g., *Fialko et al.*, 2005; *Milliner et al.*, 2015]. Numerical models show that
619 shallow slip is already reduced by 18.6 % in simulations with purely elastic material prop-
620 erties [supplemental material of *Roten et al.*, 2017]. The SSD in their simulations is fur-
621 ther increased when accounting for off-fault plasticity, but depends on the underlying
622 bulk cohesion model (higher SSD with lower rock quality). The modeled SSD on a non-
623 planar yet single fault plane model of the Landers system ranges between 42.9% (good
624 quality rock) and 28.0% (high quality rock), consistent with slip inversion results.

625 Let us compare the resulting slip distribution of our dynamic rupture model (on
626 a segmented fault system and including off-fault plasticity) to inversion results of *Gombert*
627 *et al.* [2018] and to numerical simulations on a single non-planar fault plane [*Roten et al.*,
628 2017]. Recall from Sec. 2.4 that all material properties that influence off-fault plastic-
629 ity, such as bulk cohesion and bulk friction, are constant along strike.

630 Fig. 6 shows normalized slip (bottom axis) and corresponding SSD (top axis) of
631 our simulation. The corresponding SSD quantifies the slip reduction within the first 100 m
632 from the surface with respect to the maximum slip, similar to the definition of *Roten et al.*
633 [2017]. We therefore calculate the mean slip across each fault segment in 100 m inter-
634 vals, considering only slip higher than 0.1 m, and then normalize it by the segment’s max-
635 imum slip at depth. Note that the SSD functions for different fault segments start at slightly
636 different depths since the fault surfaces intersect with the changing topography.

637 Our derived SSDs vary between 30% and 50%, with an average SSD of 41%. The
638 highest SSD is found at the CRF (50%). An SSD of 30% is found at the HVF while the
639 KF depict a SSD of 31%. Surface slip on the JVF is reduced by $\approx 49\%$ and on the EF
640 by 48%. Our results indicate that variations of the SSDs within $\approx 20\%$ are possible with-
641 out any lateral heterogeneity of bulk cohesion. Hence, spatial variations in SSD can be
642 attributed to different fault orientations and the resulting variations in dynamic rupture
643 behavior.

644 While our results agree well with the observational range of 30-60% *Gombert et al.*
645 [2018]’s Bayesian slip-inversion suggests that the maximum SSD of 50% occurred at the
646 HVF, which is underestimated in our model. In contrast, our SSD-values at the JVF and

647 EF are overestimated in comparison to the probabilistic approach of *Gombert et al.* [2018].
648 Additionally, their shallow slip at CRF is reduced by only 20%, while we observe a SSD
649 of 50%.

650 We infer a relatively high SSD of 50% across the first rupture segments, which may
651 be related to the inferred principal stress orientation. We assume that the hypocentral
652 region is well oriented with respect to the principal stress orientation leading to a large
653 amount of slip at depth. Subsequently, rupture propagates mostly along the Kickapoo
654 branch, preventing larger surface slip at the JVF. The results are independent of the nu-
655 cleation procedure initiating spontaneous rupture, as discussed in Sec. 4.1.

656 In Sec. 4.5 we further discuss the implications of our SSD estimates at the CRF
657 segment in the light of recent very low SSD estimates by *Gombert et al.* [2018] and the
658 hypothesis of shallow slip at the northern part of the fault system being triggered stat-
659 ically, shortly after the event, rather than coseismically [*Sieh, 1996; Kaneda and Rock-*
660 *well, 2009*].

661 We now compare our findings to single fault-plane simulations that include fric-
662 tional heterogeneity to approximate along-strike variations in fault strength [*Roten et al.,*
663 2017]. Their reported average SSD of 42.9% is almost identical to the inferred 41% us-
664 ing a similar cohesion model but more complex fault structures.

665 In our model, relatively high stress drops facilitate rupture transfers across geomet-
666 rical complexities. The scenario features a maximum stress drop of 33 MPa at a depth
667 of 10 km, which is slightly higher than the maximum stress drop of 25 MPa used in Landers-
668 type simulations by *Roten et al.* [2017]. The average stress drop over all positive slip re-
669 gions is 12.5 MPa. Such overall high stress drops are consistent with expectations for
670 events with long recurrence time and the inferred global averages from far-field wave-
671 forms [*Sieh et al., 1993; Kanamori et al., 1992*]. However, stress drop estimates contain
672 a large degree of uncertainty: *Sieh et al.* [1993] and *Kanamori et al.* [1992] report for in-
673 stance 20-28 MPa inferred from the ratio of radiated energy to seismic moment. An anal-
674 ysis of on-fault static stress-drop estimates from kinematic source models for the Lan-
675 ders earthquake, using the method of *Ripperger and Mai* [2004], reveals stress drop av-
676 erages over all positive slip regions of 6-12 MPa, and maximum stress changes of over
677 30 MPa within the largest asperities, consistent with our model. However, high stress
678 drops also increase the effect of plasticity, and as a consequence the reduction of shal-

679 low slip due to plastic yielding along single fault planes [Roten *et al.*, 2016]. Our model
680 indicates that similar SSD values are possible, even for scenarios with higher stress drop
681 but more complex fault geometries.

682 **3.5 Ground Motions**

683 In the following, we compare synthetic seismograms of our preferred dynamic rup-
684 ture scenario to observed waveforms and their peak ground velocities (PGVs). The sta-
685 tions used for comparison are shown in Fig. 7. Site names, V_{s30} -values, Joyner-Boore
686 distances R_{JB} , and fault-station azimuths are summarized in Table 1. Recorded accelero-
687 grams are downloaded from the strong motion data center ([http://www.strongmotioncenter.](http://www.strongmotioncenter.org/)
688 [org/](http://www.strongmotioncenter.org/)) and integrated for velocities. Note that the scope of our study is not to fine-tune
689 the model towards detailed waveform fitting. Rather, we develop a self-consistent physics-
690 based dynamic source model that generates the radiates seismic waves as a desired "by-
691 product".

692 **3.5.1 Peak Ground Velocities**

693 The Landers event is a prominent example for a strike-slip earthquake with strong
694 directivity effects, i.e. exhibiting large PGV variability with respect to the fault azimuth
695 [e.g., Vyas *et al.*, 2016]. Correspondingly, we analyze the PGVs not only in dependence
696 of R_{JB} -distance, but also with respect to azimuth to the fault.

697 We calculate PGVs using the sensor orientation independent measure GMRotD50
698 [Boore *et al.*, 2006]. Fig. 7 is an overview map of our high-resolution model region de-
699 picting synthetic PGVs exceeding 5 cm/s. The maximum simulated PGVs exceed 200 cm/s,
700 and are found in the vicinity of the HVF. We observe a clear directivity effect to the north,
701 north-north-west, while we find strong amplification of ground motions close to the Salton
702 Sea Basin and the San Bernardino Basin due to low S-wave speeds in the subsurface model
703 (see ground motions in Fig. 7).

704 Fig. 8a compares the simulated (PGV_{syn}) and the observed PGVs (PGV_{obs}) with
705 respect to R_{JB} -distance. We include the standard deviation σ -interval (gray error bars)
706 of the ground-motion prediction equations (GMPEs, gray diamond, Boore and Atkin-
707 son [2008]) for each station. The corresponding residuals ($\ln(PGV_{syn}/PGV_{obs})$) between

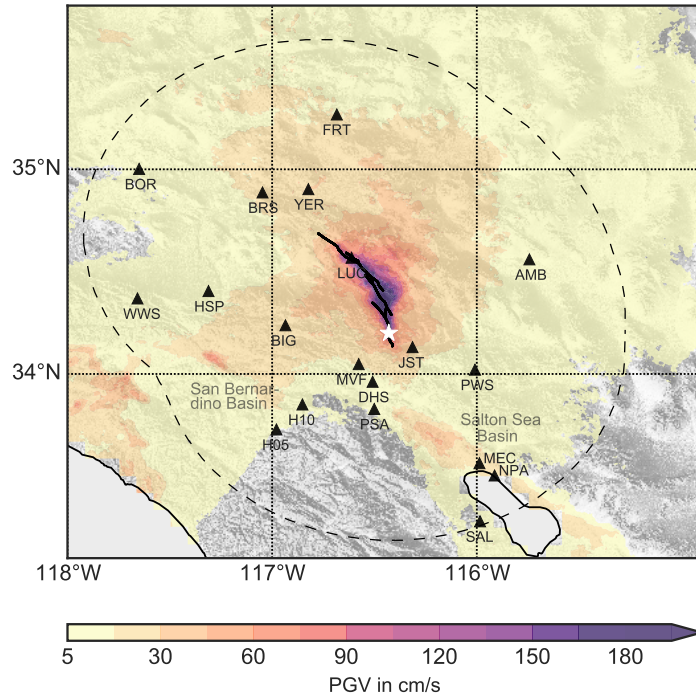
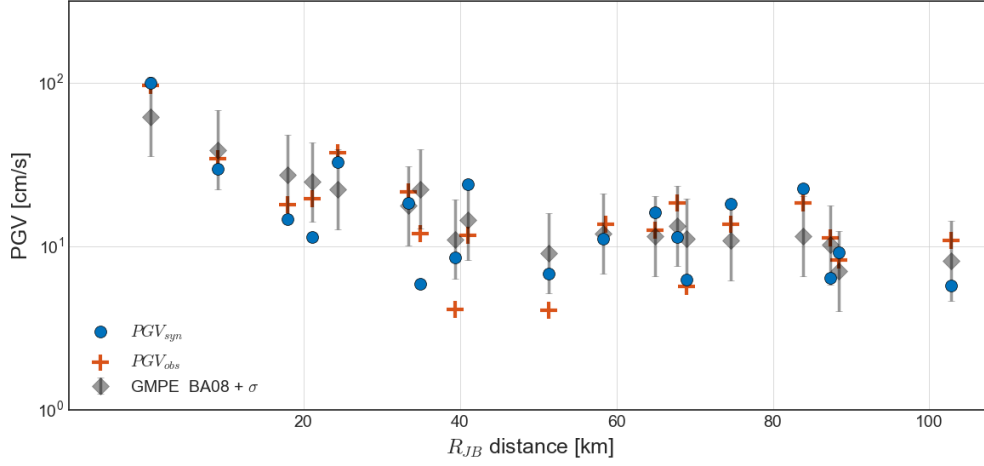


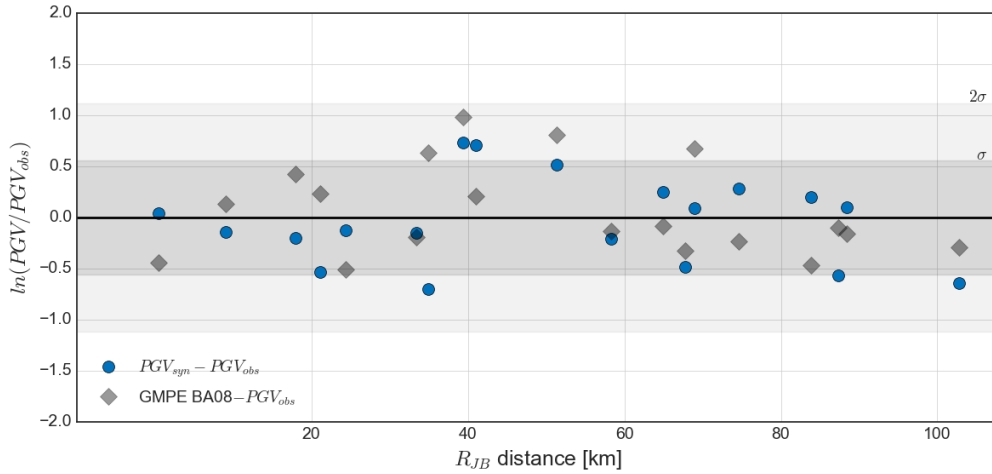
Figure 7: Overview map of the model domain, colored by the simulation’s peak ground motions above 5 cm/s based on GMRotD50 [Boore *et al.*, 2006]. The white star marks the epicenter of the 1992 Landers mainshock. Black triangles mark the seismic stations used for comparisons (for details see Table 1). The dashed line denotes the area of R_{JB} -distance of 105 km.

station	name	V_{s30} (m/s)	R_{JB} -distance (km)	azimuth ($^{\circ}$)
LUC	Lucern	685.0	0.47	-22.57
JST	Joshua Tree	379.0	9.04	144.77
MVF	Morongo Valley	345.0	17.93	-128.53
DHS	Dessert Hot Springs	345.0	21.12	-105.14
YER	Yermo	354.0	24.37	-25.03
BRS	Barstow	371.0	33.37	-36.77
PSA	Palm Springs Airport	207.0	34.88	-98.76
PWS	Twentynine Palms	685.0	39.37	153.36
BIG	Big Bear	415.0	40.98	-85.0
H10	Silent Valley	685.0	51.32	-134.99
HSP	Hesperia	371.0	58.31	-74.41
FRT	Fort Irwin	345.0	64.97	-11.36
AMB	Amboy	270.0	67.78	57.19
H05	Hemet	339.0	69.0	-134.0
MEC	Mecca	318.0	74.58	120.6
NPA	North Shore Salton Sea	265.0	83.89	122.25
BOR	Boron	291.0	87.33	-51.49
WWS	Wrightwood	506.0	88.41	-80.56
SAL	Salton City	325.0	102.8	112.49

Table 1: Stations used in this study, including site name, V_{s30} -value (used to calculate the corresponding GMPE values), Joyner-Boore distance R_{JB} , and azimuth to the fault trace. Stations are ordered with respect to R_{JB} -distance.

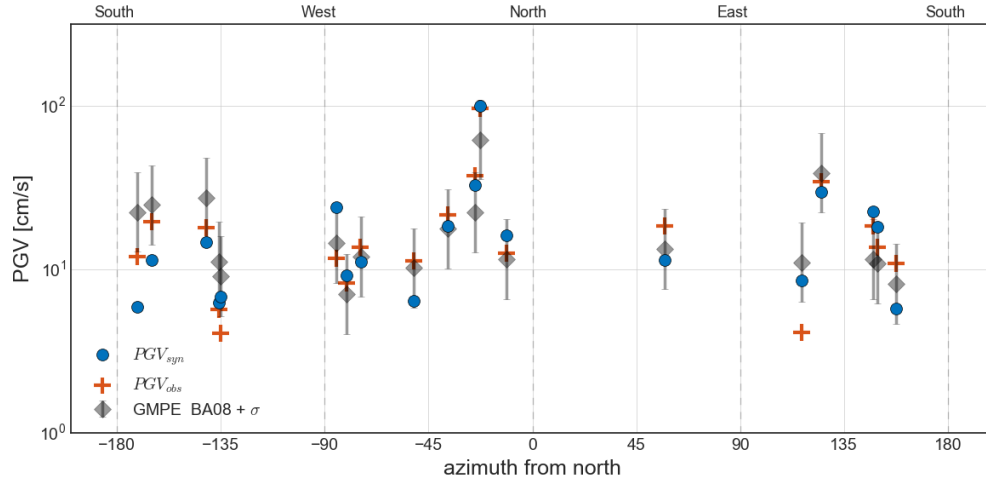


(a)

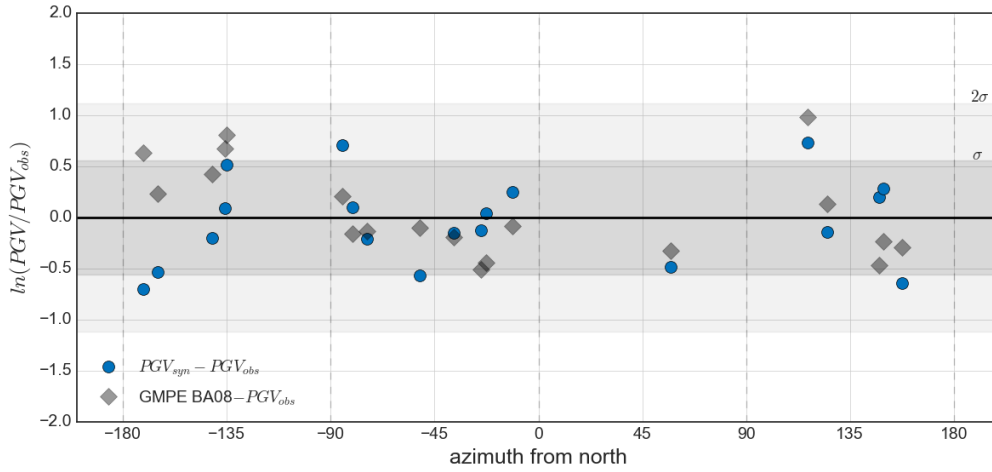


(b)

Figure 8: a) PGVs simulated (PGV_{syn} , blue) and observed (PGV_{obs} , orange) in dependence of Joyner-Boore distance R_{JB} for all stations in Fig. 7. Gray diamonds represent corresponding GMPE values [Boore and Atkinson, 2008] (including its standard deviation shown as gray bars). b) PGV-residuals, calculated as $\ln(PGV_{syn}/PGV_{obs})$ for synthetic and observed PGVs (blue dots) and $\ln(GMPE/PGV_{obs})$ for GMPE values and observed PGVs (gray diamonds). The dark and light gray shaded areas show the σ and 2σ standard deviation interval, respectively.



(a)



(b)

Figure 9: a) PGVs simulated (PGV_{syn} , blue) and observed (PGV_{obs} , orange) in dependence of fault azimuth of the stations given in Fig. 7. Gray diamonds represent the GMPE values [Boore and Atkinson, 2008] for each station (including its standard deviation shown as the gray bars). b) Corresponding residuals ($\ln(PGV_{syn}/PGV_{obs})$) for synthetic and observed PGVs and $\ln(GMPE/PGV_{obs})$ for the corresponding GMPE values. The dark and light gray shaded areas show the σ and 2σ standard deviation interval, respectively.

708 the simulated and observed PGVs, as well as between GMPEs and observed PGVs ($\ln(\text{GMPE}/\text{PGV}_{\text{obs}})$)
709 are depicted in Fig. 8b.

710 In general, our simulation results agree very well with the observed PGVs, as all
711 residuals are within two standard deviations. Particular close to the fault, our simula-
712 tion results agree better with the observations than the values inferred from GMPEs.
713 The largest residuals are found for stations within 39-51 km R_{JB} -distance (stations PWS,
714 BIG, H10, IND) for which the simulations over-predict PGV-values. These four stations
715 are all somewhat in the backward rupture directivity direction, in particular IND and
716 PWS. The back-propagating rupture on the HVF in our scenario may contribute to the
717 locally larger synthetic PGVs.

718 To analyze a potential azimuthal trend, we plot the PGV-values and correspond-
719 ing residuals with respect to fault-station azimuth (Fig. 9a and 9b). First, we clearly ob-
720 serve an underestimation of the GMPEs in forward direction, ($\approx 10\text{-}39^\circ$) as reported
721 by *Vyas et al.* [2016]. Our simulation results are much closer to observations than the
722 generic GMPEs for these stations. Simulated PGVs in forward direction show very good
723 agreement with the recorded PGVs within one standard deviation. Simulated PGVs over-
724 estimate several stations in backward direction ($> 110^\circ$), as mentioned above.

725 In summary, the peak ground velocities from our simulation results agree well with
726 observations, without any significant error trend with respect to R_{JB} -distance and fault-
727 station azimuth. The specific effects of off-fault plasticity on the synthetic peak ground
728 motions with respect to the directivity effect is described in the Discussion part (Sec.
729 4.2).

730 **3.5.2 Waveforms**

731 Next, we examine the seismic waveform characteristics of our simulations, and com-
732 pare them against observations. Fig. 10 shows three-component seismograms for a se-
733 lection of stations in forward and backward direction, as well as perpendicular to the fault,
734 ordered by R_{JB} -distance. All seismograms show velocities in cm/s, are bandpass filtered
735 between 0.05 Hz and 1.0 Hz, and are normalized by their maximum value (annotated
736 above the time series). Some of the observational strong motion recordings lack exact
737 timing information, hence, we cross-correlate them with our synthetics for temporal align-
738 ment.

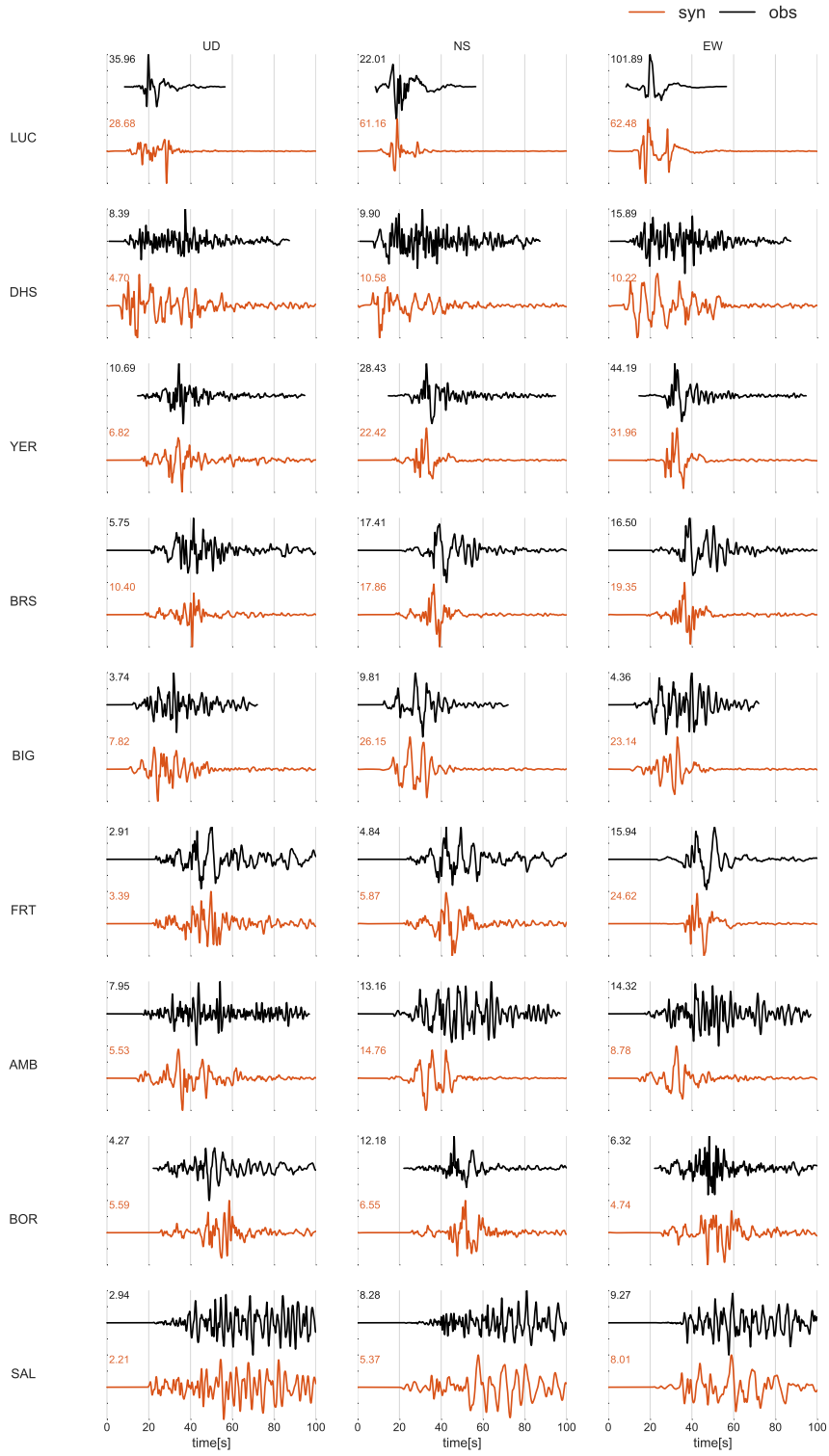


Figure 10: Observed (orange) and simulated (black) seismic velocities in cm/s for a selection of stations (Fig. 7). All seismograms are bandpass filtered between 0.05 and 1 Hz. The waveforms are normalized by their maximum value (stated above each trace) to facilitate comparison and ordered by their R_{JB} -distance.

739 The waveform comparisons show very good agreement between simulations and ob-
740 servations, although not all details of the recordings are reproduced. However, this does
741 not come as a surprise, because our study does not attempt to find an optimized source
742 parameterization to fit waveforms (like in a source inversion study). Still, our synthetic
743 waveforms capture the main S-wave pulses, amplitudes, and shaking duration, indicat-
744 ing not only the quality of dynamic rupture model, but also of the numerical method used.

745 In the forward direction, the main velocity pulses at stations YER and BRS are
746 very well reproduced. At YER, waveform characteristics and amplitudes agree very well
747 on all three components. For BRS, both horizontal components are very consistent, while
748 for the vertical component the synthetic waveform is substantially larger. For these two
749 stations we also notice that our simulations are not quite able to reproduce the coda-
750 wave behavior following the main pulses, possibly due to the influence of unmodeled small-
751 scale heterogeneity that leads to seismic scattering. This changes, to some extent, for
752 the farther-away stations BOR and FRT. Both are located north of the fault but not ex-
753 actly in the expected forward-directivity cone. In both cases, the synthetics well repro-
754 duce not only the dominant source-related S-wave pulses (of about 5 sec duration), but
755 also the later part of the waveforms (at least in a statistical sense). On all three com-
756 ponents, the amplitudes are very well matched at stations BOR and FRT.

757 In backward direction (i.e. to the south of the fault system), we obtain good agree-
758 ment at station DHS for an ≈ 10 sec long source-dominated shear-wave that arrives in
759 two distinct wave packages (spaced about 6-7 sec apart). Amplitudes match reasonable
760 well, but coda-waves (due to scattering) are not well reproduced. A similar pattern evolves
761 for stations to the east of the fault (e.g., AMB) and to the west (e.g., BIG). The source-
762 dominated shear-waves are in excellent agreement (though the amplitudes of the syn-
763 thetics at BIG are higher by a factor 2-5), while the coda behavior is not well reproduced.

764 Scattering caused by topography and a smooth 3D Earth model is insufficient to
765 generate realistically scattered waves [*Imperator and Mai, 2015*]. Interestingly, however,
766 the farthest recording (at SAL) demonstrates a very consistent overall waveform char-
767 acter, including the coda waves. Source-related wave packets are barely visible here, since
768 regional wave-propagation effects dominate, including significant topographic changes
769 and the sedimentary basin of the Salton Sea.

770 The closest station to the fault trace, Lucerne station (LUC), recorded strong mo-
771 tions in only 470 m distance from our modeled fault trace of the EF. We note, that the
772 waveform in the synthetic seismogram does not align with observations, in contrast to
773 the synthetics for other stations in forward direction (such as YER and BRS). Addition-
774 ally, the amplitude on the north-south (NS) component of LUC is over-predicted by our
775 simulations, while the east-west (EW) component is underpredicted (in each case about
776 a factor 2). We hypothesize, that part of these discrepancies are caused by rotational com-
777 ponents of the wave field. Particularly near-source strong motion accelerometers may
778 be distorted by rotational motions of the sensor during coseismic slip [e.g., *Graizer*, 2005].
779 This subsequently impacts recordings upon integrating to velocities.

780 3.6 Off-fault Deformation

781 During earthquake rupture, the released energy is not only accommodated by fric-
782 tional sliding on the fault and radiated seismic waves, but is also absorbed by inelastic
783 processes such as plastic deformation in the vicinity of the fault. Off-fault deformation
784 thus poses a key component in the energy budget of earthquakes [e.g., *Rice et al.*, 2005;
785 *Kanamori and Rivera*, 2006]. Relationships between the width of the damage zone and
786 fault displacement provide helpful insight into the associated fault growth and rupture
787 processes [e.g., *Faulkner et al.*, 2011].

788 *Milliner et al.* [2015] correlate pairs of aerial photographs before and after the 1992
789 Landers earthquake to map co-seismic off-fault deformation. The corresponding fault zone
790 width is defined as the perpendicular extend of surface shear to either side of the fault.
791 They find that the magnitude and width of the mapped off-fault deformation correlates
792 with geometrical complexity of fault surface traces.

793 Fig. 11 compares the accumulated plastic strain distribution in our simulation with
794 fault zone width (FZW) measurements [*Milliner et al.*, 2015]. Here, we focus on the qual-
795 itative characteristics of the synthetic plastic strain distribution and its relation to fault
796 geometry, as the numerical resolution does not allow for quantitatively translating the
797 dynamically induced plastic strain fields into mapped fault damage zones. Our simula-
798 tion reproduces key features of the mapped fault zone width, in particular the drastic
799 increase of off-fault damage in geometrically complex fault regions.

800 Following the fault trace from south to north, an increase of FZW for both the mapped
801 and simulated damage zones can be observed, particularly at the southernmost part of
802 the JVF. Close to the branching point to the KF, our model predicts an increase in plas-
803 tic deformation on the extensional side of the fault which agrees with the FZW of *Milliner*
804 *et al.* [2015]. The region with highest plastic strain between 3800-3810 km UTM Nor-
805 thing is clearly correlated with the observed increase of the FZW. Although the south-
806 ernmost part of the EF did not fully rupture in the simulation, shallow fault slip still trig-
807 gers plastic deformation very narrowly around the fault trace. Both models show an in-
808 crease in fault zone complexity at the transition of the HVF and EF (see inset to Fig.
809 11). In particular, the dynamic rupture scenario reveals how the accumulated plastic strain
810 connects the ends of the HVF and the EF. The northernmost part of the fault system
811 lacks off-fault plastic deformation, owing to the lack of shallow slip at the CRF.

812 An observed increase of the FZW close to the hypocenter suggests that the fault
813 zone structure may be locally more complex than our modeled fault-surface represen-
814 tation. Accounting for a more complex geometry would potentially slow down rupture
815 and/or reduce the energy release at the JVF [*Zielke et al.*, 2017] (see also Sec. 4.1). Small-
816 scale fault roughness, as observed for natural faults [e.g., *Candela et al.*, 2012], is not in-
817 cluded in our model, but potentially may lead to a strong signature in the simulated plas-
818 tic deformation [*Dunham et al.*, 2011a; *Shi and Day*, 2013].

819 At the transition between the HVF and EF, our model accounts only for one branch,
820 while fault trace mapping shows two subsequent branches to the EF [*Sieh et al.*, 1993;
821 *Milliner et al.*, 2015]. The increase of plastic strain at the HVF results in a rapid decrease
822 of rupture speed in the vicinity of its geometrical barrier (fault bend). Interestingly, this
823 plastic strain exactly connects the HVF and EF where the second branch is observed.
824 Hence, this connection may have been created or enhanced during the 1992 Landers event.

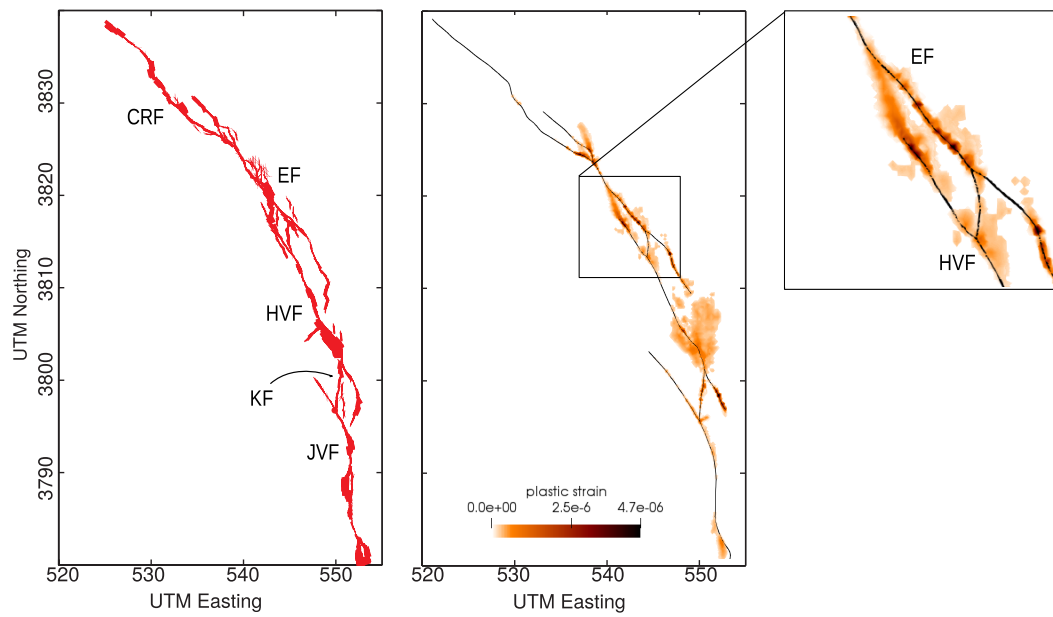


Figure 11: Fault zone width (FZW) compiled by *Milliner et al.* [2015] from aerial photograph correlations (left) in comparison to the accumulated plastic strain from the presented dynamic rupture simulation (middle). The right figure shows an inset at the transition from the HVF to EF.

4 Discussion

Sustained rupture along the geometrical complex fault of the 1992 Landers earthquake provides strong constraints on the model parametrization such as stress orientation, stress amplitudes and friction. Our source model shows excellent agreement with estimated moment-release rate, recorded PGV's, and key features of the observed off-fault deformation patterns. We discuss in the following further implications, potential improvements, but also the sensitivity to variations in prior assumptions of the preferred dynamic rupture model (hereafter named the reference simulation).

4.1 Early moment release and earthquake initiation

The presented Landers earthquake scenario slightly overestimates moment release within the first 10 s (Fig. 5) compared to the SCARDEC solutions [Vallée and Douet, 2016]. The higher moment release occurs during nucleation, rupture across the JVF and branching into the KF. We here discuss potential reasons and improvements specifically with respect to earthquake nucleation and the parametrization of the first segments of the fault system.

Dynamic rupture simulations are initiated by an artificial nucleation procedure on a pre-defined nucleation patch (see Sec. 2.3). In our simulation, this leads to a rapid start of rupture, which is further enhanced by the favorable orientation of the hypocentral fault region with respect to the regional stress field. However, observations indicate that rupture started gradually during the first 3 seconds, likely due to a small foreshock in the vicinity of the epicenter [e.g., Campillo and Archuleta, 1993; Abercrombie and Mori, 1994].

In our modeling, we find that rupture dynamics and associated moment release remain robust across the first fault segment when varying nucleation patch size, forced rupture time or forced rupture speed within the nucleation patch. This allows to also examine if the prescribed nucleation procedure affects spontaneous rupture behavior at the JVF. Spontaneous rupture is delayed, but still initiates for radii as small as 0.5 km. For larger radii (up to 4.5 km), rupture initiates faster, however, the moment-release rate remains unchanged. Similar behavior is found for varying the time of the forced nucleation t_{nuc} : for shorter nucleation times (0.2 s) rupture initiates faster, but spontaneous rupture outside the nucleation patch is identical. We find that rupture speed and moment-

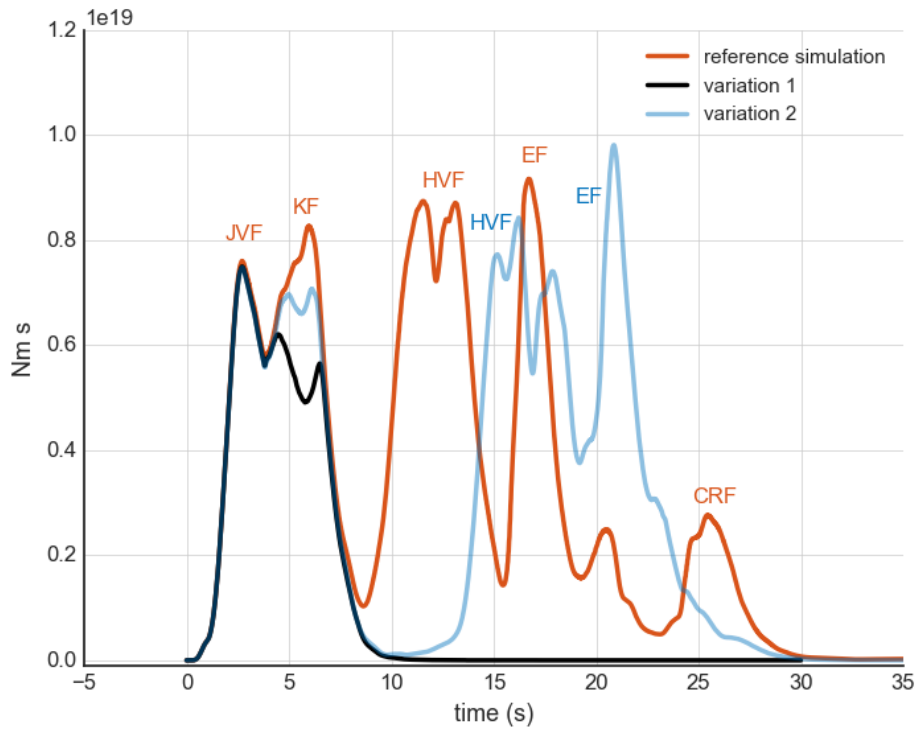


Figure 12: Seismic moment-release rate of the reference simulation (orange) in comparison to two models with changed principal stress orientation governing the KF: Model variation 1 (black) assumes a linear transition of the stress regime of the JVF to the HVF (33° to 20°) starting at the beginning of the KF and ending at the intersection with the HVF. Model variation 2 (light blue) features the same transition to 20° at the HVF but starting in the center of the KF.

855 release rate outside the nucleation patch are not changed by varying the forced rupture
 856 speed within the nucleation patch v_{nuc} in the range of 2000 m/s to 3300 m/s.

857 Mapped surface traces and off-fault deformation distributions indicate that struc-
 858 tural complexity is enhanced close to the hypocenter [Liu et al., 2003; Milliner et al., 2015].
 859 The rapid rupture initiation could potentially be delayed by considering fault structures
 860 more complex than the curved, yet purely strike-slip fault geometry used in our simu-
 861 lation. Including small-scale geometrical roughness may additionally slow down rupture
 862 and limit the stress drop [Dunham et al., 2011b; Shi and Day, 2013; Zielke et al., 2017;
 863 Mai et al., 2017], while simultaneously increasing off-fault damage.

864 The 5 km short connecting Kickapoo fault (KF) plays a crucial role for early moment
865 release by linking the Johnson Valley (JVF) and Homestead Valley (HVF) faults.
866 Despite its short length, it slipped with a maximum of nearly 3 meters, and may have
867 hosted the initiation of the March 15, 1979, Homestead Valley earthquake [*Hill et al.*,
868 1980; *Sowers et al.*, 1994]. However, local principal stress orientation are not well con-
869 strained, since it is debated whether this fault branch is part of the San Bernardino or
870 the Central Mojave domain.

871 We observe a second relatively high peak of moment-release rate at around 6 s (see
872 Fig. 12) related to slip at the KF. Decreasing the angle of principal stress orientation
873 acting on this fault step-over branch reduces this peak. In our reference model (Sec. 2.2),
874 the KF experiences an equivalent angle of maximum compressive stress (33°) as the JVF.
875 However, if the KF already constitutes the transition between the San Bernardino and
876 the Central Mojave domains, its local stress orientation might be steeper.

877 Therefore, we test two variations in stress orientations across the KF, which respec-
878 tively vary its strength. First, background stresses smoothly rotate from 33° , starting
879 at the beginning of the KF and reaching 20° at the intersection with the HVF (model
880 variation 1). The black line in Fig. 12 demonstrates the reduced moment-release rate
881 between 4-7 s, related to rupture on the KF, for this case. However, subsequently rup-
882 ture is coming to a complete halt at the JVF, and thus is unable to propagate across the
883 remaining fault segments.

884 Second, we test the hypothesis that the initial part of the KF is favorably oriented
885 (33° , to promote branching), while stresses start to rotate to 20° only in the center of
886 the KF (model variation 2, light blue line in Fig. 12). In this case, the moment-release
887 rate between 4-7 s is still decreased with respect to the reference model, but not as pro-
888 nounced as for model variation 1. Rupture initiation at the HVF is drastically delayed
889 - by 5.5 s in comparison to the reference model. After re-initiation, rupture overcomes
890 the fault-bend barrier and breaks the entire fault system. The rupture path is very sim-
891 ilar to the reference model, highlighting the robustness of the source dynamics described
892 in Sec. 3.1.

893 Our numerical experiments therefore suggest a locally steeper angle of principal
894 stress orientation in order to better match the estimated moment-release rate within the
895 first 10 s of rupture. However, such principal stress orientation may require other mech-

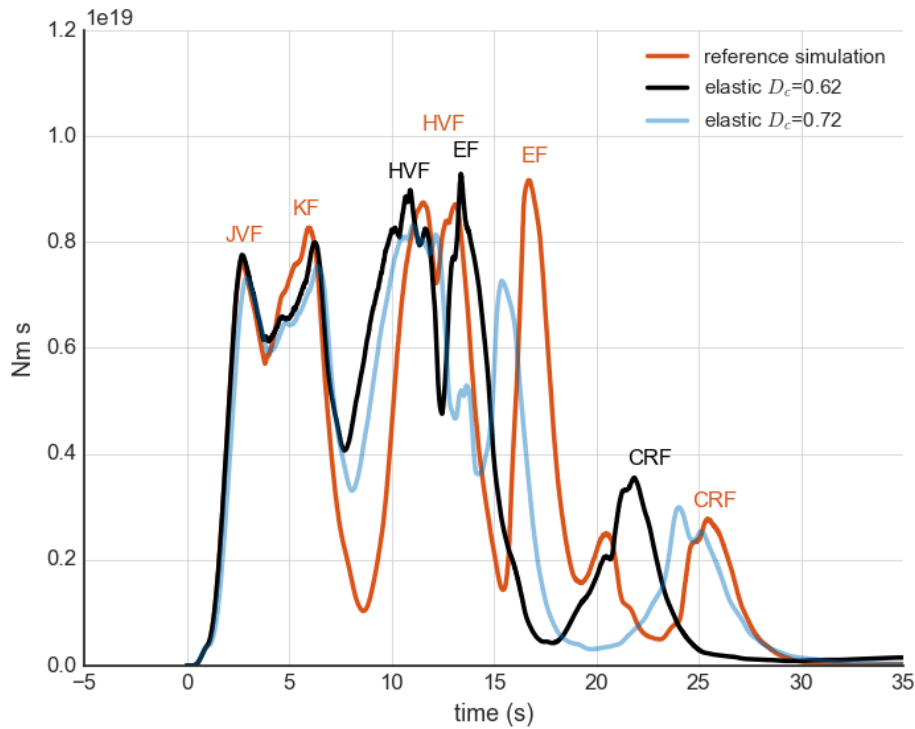


Figure 13: Seismic moment-release rate of the reference simulation including off-fault plasticity (orange), compared to an identically parametrized but purely elastic simulation (black), and an elastic simulation with a higher critical slip distance D_c (light blue).

896 anisms facilitating rupture transfers, such as: i) more complex fault geometries, includ-
 897 ing additional connecting fault segments as seen in fault traces by *Liu et al.* [2003], ii)
 898 fault weakening mechanisms, such as strong velocity-weakening friction or the effect of
 899 thermal pressurization, since there is evidence of a fluid-saturated upper crust, [*Fialko,*
 900 2004b], iii) compliant fault zones with reduced rigidity promoting rupture propagation
 901 [*Finzi and Langer, 2012a*]. Investigating the effects of these physical mechanisms on the
 902 dynamic rupture process of the Landers earthquake will be hopefully addressed in fu-
 903 ture work, but is beyond the scope of this study.

4.2 The Effect of Off-fault Plasticity on Rupture Transfer and Moment Rate

In nature, high stresses during earthquake rupture are accommodated by inelastic processes near the crack tip, but also in the bulk, such as plastic deformation of the host rock. *Wollherr et al.* [2018] demonstrate the influence of non-elastic material behavior on the spatio-temporal rupture transfer processes across the geometrical complexities of the Landers fault system. Plastic strain accumulates when the rupture path deviates from planarity, e.g., at changes of fault strike orientation, branching, or segment endings, and is associated with strong reduction in peak slip rate (up to 50%). Off-fault plasticity also delays rupture arrivals across the entire fault, even to a larger extent than reported for scenarios on planar faults [*Roten et al.*, 2015]. In direct comparison of purely elastic scenarios and those including plasticity, slip is found to be locally higher but more concentrated. As a result, moment magnitudes are comparable with and without plasticity, even though the rupture path differs dynamically.

We now compare the results of our reference model that includes off-fault plasticity to simulations with purely elastic material properties, and discuss the effect of off-fault deformation on moment-release rate and rupture transfer on this complex-fault system. Fig. 13 depicts the moment-release rate of our reference simulation (orange) to an equivalent scenario assuming purely elastic material response (black, labeled with $D_c=0.62$). The model parameterization is otherwise exactly the same. The resulting seismic moment is $M_0^{ela} = 11.102e+19$ Nm ($M_w^{ela} 7.292$), compared to $M_0 = 11.106e+19$ Nm ($M_w 7.293$) of the reference simulation with off-fault plasticity.

While the overall seismic moment is almost identical for both cases, the moment release is distributed slightly differently during the intermediate rupture stage: We find that rupture transfers across geometrical barriers are generally enhanced if off-fault plasticity is neglected. The rupture transfer between the KF and the HVF is facilitated by the purely elastic material response (at 11 s in Fig. 13), and rupture also transfers faster between the HVF and EF, leading to a smaller gap in moment rate release (at 12 s). Consequently, rupture at the CRF is initiated ≈ 5 s earlier than in the simulation with off-fault plasticity (compare the last moment rate peak for both scenarios).

Interestingly, our numerical tests reveal that fully elastic simulations can partially emulate the reference simulation when increasing the critical slip distance D_c . In this

936 case, moment-release rate and rupture transfer dynamics are preserved, but exhibit slower
937 rupture speeds and longer delays when transferring to adjacent segments due to an in-
938 creased critical size [e.g., *Ampuero et al.*, 2002; *Bizzarri*, 2010; *Galis et al.*, 2014] to ini-
939 tiate self-sustained rupture by dynamic triggering.

940 For simulations based on linear slip weakening friction including off-fault plastic-
941 ity (i.e. the reference case), we find that both, relatively high stress drops and a rela-
942 tively low critical slip distance of $D_c = 0.62$, are required to sustain rupture along the
943 segmented faults. In particular, the geometrical barrier at the center of the HVF, as well
944 as the transition between the HVF and the EF, pose strong boundary conditions for sus-
945 tained rupture. When increasing only as much as to $D_c = 0.64$ we observe rupture de-
946 lays of more than 5 s between the KF and the HVF. For values of $D_c > 0.64$ we ob-
947 serve a complete stop of rupture before breaking all segments.

948 In the corresponding elastic simulations, rupture transfers are facilitated by the lack
949 of plastic deformation in the vicinity of geometrical barriers [e.g., *Wollherr et al.*, 2018].
950 For example, by increasing D_c to 0.72 in the elastic simulation (i.e. increasing the frac-
951 ture energy by 16%), rupture and the transition between distinct fault segments are dis-
952 tinctly slowed down (see light blue line in Fig. 13). However, the resulting seismic mo-
953 ment of $M_0^{ela} = 10.057e+19$ Nm ($M_w^{ela} 7.279$) is very similar to the seismic moment of
954 the reference simulation.

955 4.3 The Effect of Off-fault Plasticity on Peak Ground Motions

956 Let us examine the effects on peak ground motions for these three scenarios. Ground
957 motions in seismic hazard assessment are typically described by Ground Motion Predic-
958 tion Equations (GMPEs) that depend mainly on event magnitude, source-to-site distance,
959 and site-effects (e.g. the V_{s30} -value), but other source-related and path-related effects
960 may be important, too. However, standard GMPEs fail to describe ground motions of
961 earthquakes with strong directivity effects, varying rupture speed or 3D velocity struc-
962 tures including low-velocity basins [e.g., *Graves et al.*, 2008; *Spudich and Chiou*, 2008;
963 *Ramirez-Guzman et al.*, 2015]. Therefore, dynamic rupture simulations like ours are use-
964 ful to possibly complement GMPEs by exploring physically possible parameter spaces.

965 Ground motions in dynamic rupture simulations on single faults are reduced by off-
966 fault plastic yielding [*Roten et al.*, 2014, 2015], however, the combined effects of plastic

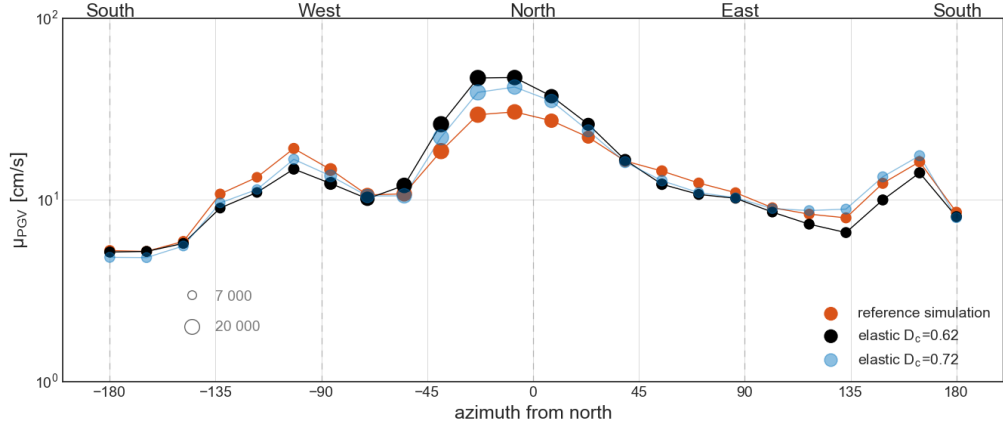


Figure 14: Azimuthal dependence of a) mean PGV denoted as μ_{PGV} for the reference simulation (orange), the corresponding elastic simulation (black) and the elastic simulation with increased D_c (light blue) for all stations between 1 km and 105 km R_{JB} -distance (bin width = 20 km). The circle radii represent the number of stations in each bin.

967 deformation, physics-based dynamic rupture transfers, and directivity on the ground mo-
 968 tion properties for complex-geometry faults has not yet been analyzed. For this purpose,
 969 we examine the mean peak ground motions and their variability for the three scenarios
 970 discussed above. The corresponding PGV maps can be found in Appendix C: .

971 **4.3.1 Azimuthal Dependence of PGVs**

972 First, we analyze the dependence of peak ground velocities (PGVs) on receiver-epicenter
 973 azimuth to help understand directivity effects in our simulations. Off-fault plasticity re-
 974 duces the mean PGVs mainly in forward direction, while they are increased in backward
 975 direction. This effect can be only partially mitigated by decreasing the rupture speed
 976 (e.g., by increasing D_c) in purely elastic simulations.

977 We calculate the PGVs of 250 000 synthetic stations distributed within 1 km and
 978 105 km R_{JB} -distance of the fault trace using GMRotD50 [Boore *et al.*, 2006]. These sta-
 979 tions are binned with respect to their azimuth to the epicenter with a bin width of 15° ,
 980 resulting in at least 7000 stations per bin.

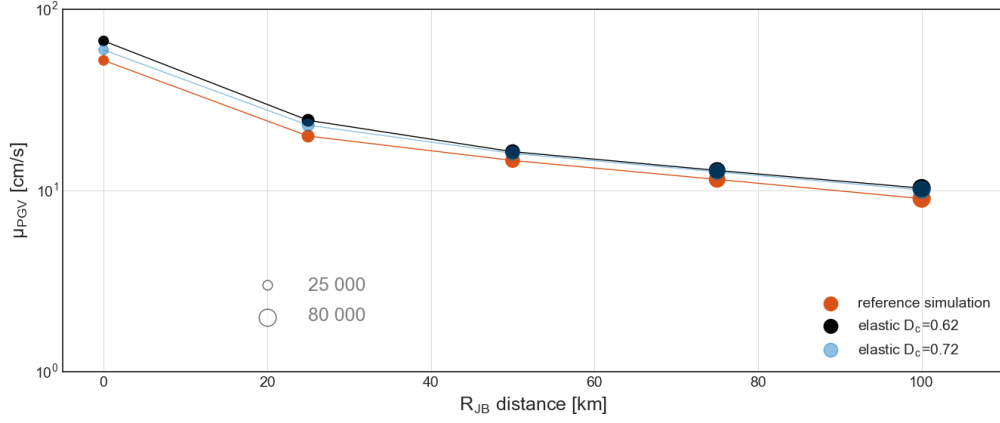
981 Fig. 14 shows the azimuthal dependence of the mean value of PGVs μ_{PGV} cal-
 982 culated for each bin and for all three scenarios. We observe differences in absolute PGVs
 983 between our scenarios, especially in the forward and backward directions. The purely
 984 elastic simulation with $D_c = 0.62$ (black) exhibits the highest μ_{PGV} reaching up to 47.1 cm/s
 985 in forward direction (between -30° and -15°). The increase of D_c from 0.62 to 0.72 m
 986 decreases μ_{PGV} by up to 11% in forward direction. Plasticity reduces μ_{PGV} by up to
 987 35% compared to an identical elastic simulation with $D_c = 0.62$ m. However, the direc-
 988 tions between -90° and -45° and 45° and -135° experience very similar μ_{PGV} for all three
 989 scenarios. In backward direction (between 150° and 165°), μ_{PGV} is elevated and peaks
 990 for the simulation with off-fault plasticity and the elastic simulation with increased D_c .

991 While some of the increase of μ_{PGV} in backward directivity is attributed to the
 992 low velocity basin around the Salton Sea that generates basin-amplification effects (see
 993 Fig. 7), we can also attribute our results to the geometrical complexity of the fault sys-
 994 tem. Rupture propagation is slowed down at geometrical barriers or fault branches by
 995 the occurrence of plastic yielding which leads to an increase of reversely propagating rup-
 996 ture. We observe that lower rupture speeds and longer delays at geometrical barriers lead
 997 to more backward traveling seismic waves which further increase PGVs in backward di-
 998 rection.

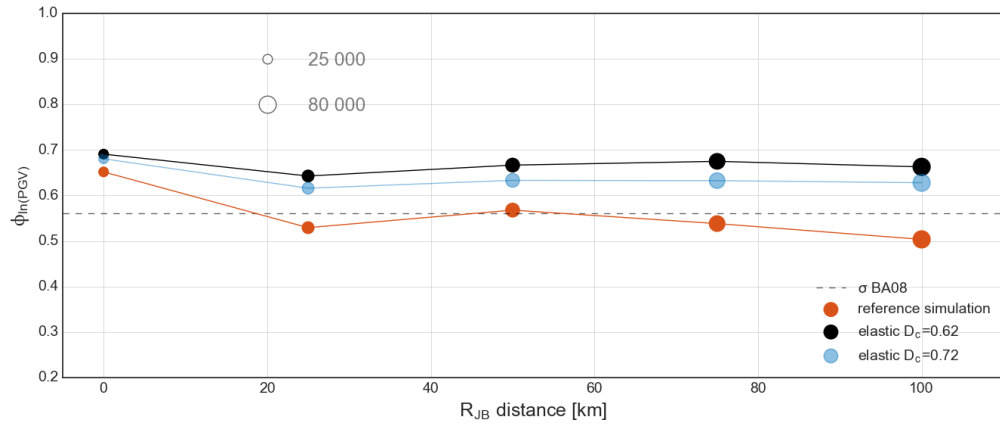
999 We conclude that the effect of plasticity can only be partially emulated by a rup-
 1000 ture speed decrease (e.g. increasing D_c) in purely elastic simulations: the simulation with
 1001 plasticity and the elastic simulation with increased D_c show similar μ_{PGV} between -180°
 1002 and -45° and 45° and 180° , but the purely elastic simulation still overestimates the di-
 1003 rectivity effect between -45° and 45° .

1004 *4.3.2 Distance Dependence of PGVs*

1005 Let us now investigate the distance dependence of the mean PGVs μ_{PGV} for the
 1006 three simulations. Plastic yielding primarily appears in the vicinity of the fault, but cor-
 1007 responding PGV maps show PGV reductions (beyond the standard geometrical spread-
 1008 ing) over large distances [Roten et al., 2014]. Interestingly, this effect has not yet been
 1009 analyzed systematically. For this purpose, stations are binned with respect to their R_{JB} -
 1010 distances using a bin widths of 20 km (at least 25 000 stations per bin). Fig. 15a shows
 1011 the mean PGV μ_{PGV} for each of these bins.



(a)



(b)

Figure 15: Distance dependence of a) the mean PGV μ_{PGV} and b) standard deviation $\phi_{\log(PGV)}$ for the reference simulation with plasticity (orange), the corresponding elastic simulation (black) and the elastic simulation with increased D_c (light blue) for all stations between 1 km and 105 km R_{JB} -distance (bin width = 20 km). The circle size represents the number of stations in each bin. The dashed line in b) represents the constant standard deviation of the GMPE of *Boore and Atkinson* [2008].

1012 In general, the elastic simulations show higher μ_{PGV} over all distances in compar-
 1013 ison to the reference simulation with plasticity. Larger differences are visible close to the
 1014 fault where plasticity reduces μ_{PGV} by 21.9% within the first 20 km, while μ_{PGV} is
 1015 reduced by on average 12.4% between 85 km and 105 km R_{JB} -distance. By increasing
 1016 D_c in the purely elastic simulations, μ_{PGV} is reduced by 10.8% within the first 50 km
 1017 (still 12.4% difference to the simulation with plasticity), but shows almost identical be-
 1018 havior for larger distances compared to the elastic simulation with $D_c = 0.62$ m.

1019 GMPEs commonly assume a constant ground motion variability [Boore and Atkin-
 1020 son, 2008], independent of the distance to the fault. However, a distance dependent vari-
 1021 ability is found for kinematic simulations of the Landers earthquake assuming purely elas-
 1022 tic material properties [Vyas et al., 2016]. Different ground motion variability values might
 1023 have a significant impact on the results of seismic hazard analysis [e.g., Restrepo-Velez
 1024 and Bommer, 2003; Bommer and Abrahamson, 2006; Strasser et al., 2009]. Here, we ad-
 1025 ditionally investigate the distance dependence of ground motion variability in dynamic
 1026 rupture simulations on complex faults including off-fault plasticity.

1027 Fig. 15a shows the standard deviation of the logarithmic PGVs $\phi_{\log(\text{PGV})}$ for each
 1028 bin in comparison to the constant value of 0.56 used by the GMPE of Boore and Atkin-
 1029 son [2008]. The variability is in general higher than 0.56 for the purely elastic simula-
 1030 tions although $\phi_{\log(\text{PGV})}$ is already reduced by 4.4% in average when we increase D_c .
 1031 The simulation with plasticity shows the smallest ground motion variability, ranging from
 1032 0.65 (0-20 km bin) to 0.50 (85-105 km bin), very close to what is used in GMPEs by Boore
 1033 and Atkinson [2008]. In the simulation with plasticity, high stresses are limited by plas-
 1034 tic yielding, which results in a reduction and smoothing of on-fault slip rates [e.g., Woll-
 1035 herr et al., 2018]. As a consequence of the smoother peak slip rates, the resulting ground
 1036 motions have lower variability.

1037 Overall, we observe only a small distance dependence of ground motion variabil-
 1038 ity for the simulations using purely elastic rock properties, in contrast to what is reported
 1039 by Vyas et al. [2016]. However, they employ kinematic source models of the 1992 Lan-
 1040 ders earthquakes using a second order accurate generalized finite-difference code [Ely et al.,
 1041 2008]. They find that the variability is much higher close to the fault (in average 0.79),
 1042 and reduces to a constant value of 0.6 only at 100 km distance (Fig. 5 in Vyas et al. [2016]).

1043 We argue that the smoother final slip distribution of our dynamic rupture source
1044 models is responsible for the lower variability of simulated ground motions. In our model,
1045 the highest slip is always located at depth, and it is very smoothly distributed across the
1046 fault segments (Fig. 4). In contrast, *Vyas et al.* [2016] use kinematic source models of
1047 *Cotton and Campillo* [1995]; *Hernandez et al.* [1999]; *Zeng and Anderson* [2000]; *Wald*
1048 *and Heaton* [1994] and *Cohee and Beroza* [1994] which all feature very heterogeneous
1049 slip distributions, that is, slip occurs in isolated patches. Also, four out of their five mod-
1050 els contain zones of large near-surface slip that may lead to an increased variability of
1051 ground motions in the vicinity of the fault. *Vyas et al.* [2016] observe the lowest distance
1052 dependence of variability for the kinematic source model of *Zeng and Anderson* [2000]
1053 that has its highest slip at depth, similar to our simulations.

1054 In contrast to the purely elastic simulation, ground motion variability close to the
1055 fault for the reference simulation with plasticity is increased by 29.4% with respect to
1056 variability between 85 km and 105 km R_{JB} -distance. Localized plastic deformation (see
1057 Fig. 11) additionally alters PGVs very heterogeneously in the vicinity of the fault, there-
1058 fore further increasing the variability within the first 20 km.

1059 We conclude that mean peak ground motions are stronger reduced in the vicinity
1060 of the fault when accounting for off-fault plastic yielding, but the reduction is still vis-
1061 ible at 100 km R_{JB} -distance. Additionally, ground motion variability for the reference
1062 simulation using off-fault plasticity is close to what is commonly used in GMPEs [*Boore*
1063 *and Atkinson*, 2008], and in general lower than in the elastic simulations. Due to the het-
1064 erogeneous distribution of near-fault plastic yielding, ground motion variability in the
1065 simulation with off-fault plasticity are slightly increased within 20 km to the fault.

1066 4.4 The Effect of Attenuation on Dynamic Triggering

1067 Viscoelastic attenuation is an important physical mechanism that describes the grad-
1068 ual damping of high frequency seismic waves with propagation distance. Our reference
1069 scenario accounts for viscoelastic-plastic rheology. We clearly observe decreasing peak
1070 velocities with increasing travel distances in comparison to a setup without attenuation
1071 (see Fig. D.1 in Appendix D: for synthetic PGVs of all seismic stations without and with
1072 accounting for seismic attenuation). However, as a consequence of the damping of the

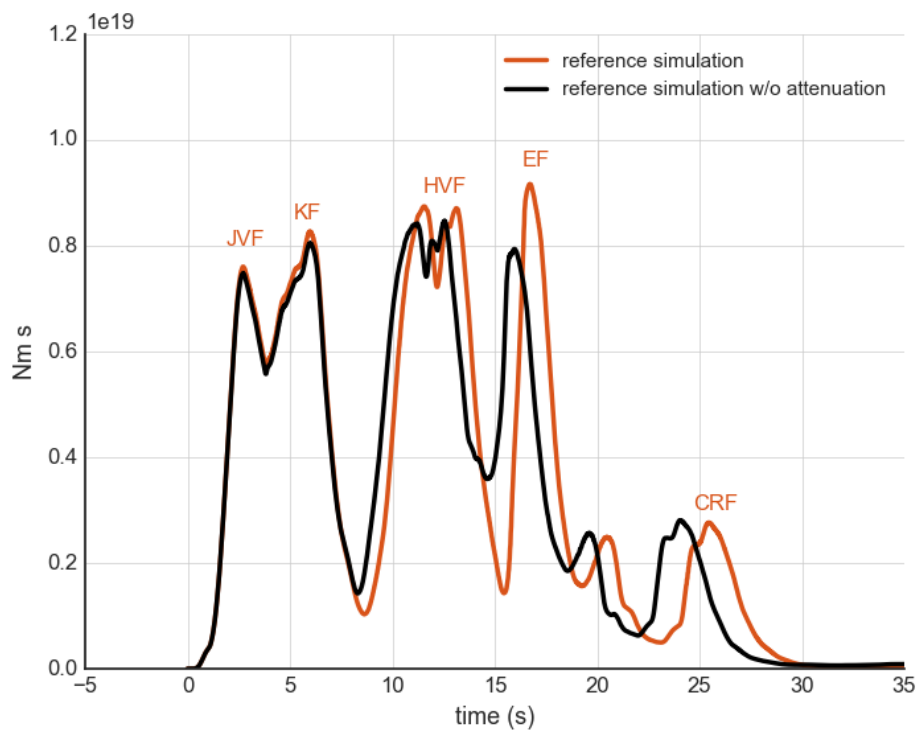


Figure 16: Seismic moment-release rate of the reference model including off-fault plasticity and viscoelastic attenuation (orange) in comparison to the corresponding simulation accounting for off-fault plasticity but not for viscoelastic attenuation (black).

1073 high frequency seismic waves, seismic attenuation also affects rupture dynamics, specif-
1074 ically the dynamically triggered rupture transfers and re-initiation.

1075 We find that all rupture transfer processes of our extended fault system are affected
1076 by the energy the seismic waves carry - no attenuation meaning more seismic energy and
1077 thus facilitation of dynamic triggering. Fig. 16 shows the moment rate over time of the
1078 reference simulation (orange) compared to the same simulation but without accounting
1079 for seismic attenuation (black). Within the first 8 s rupture propagation and moment
1080 rate release are identical. At 8.1 s, after the rupture delay at the HVF central fault bend,
1081 we observe faster rupture re-initiation in the simulation without attenuation. Addition-
1082 ally, rupture is dynamically triggered at the EF at an earlier time (at 15 s). With at-
1083 tenuation, rupture jumping to the CRF is additionally delayed (from 17.9 to 22 s).

1084 The faster rupture initiation after the bend at the center of the HVF in the sim-
1085 ulation without attenuation suggests that rupture transfer is facilitated by the non-damped
1086 arriving seismic waves. We note, that dynamic triggering in a segmented fault system
1087 is highly non-linear and may bridge distances larger than expected from simplified se-
1088 tups [*Harris and Day, 1993; Oglesby, 2008; Finzi and Langer, 2012b*]. For instance, at
1089 the northern most segments which are affected by seismic waves traveling more than 50 km
1090 from the hypocenter remote triggering is delayed with attenuation. Still, the resulting
1091 slip distribution and moment magnitude is in both cases identical (M_w 7.29). A detailed
1092 analysis of the frequency bands responsible for remote triggering of rupture at adjacent
1093 fault segments will be considered in future work.

1094 Without off-fault plasticity, rupture dynamics are less altered by ignoring atten-
1095 uation. This suggests, that near fault plastic deformation here considerably increases the
1096 uniqueness of conditions allowing sustained rupture; as a consequence dynamic trigger-
1097 ing, and an exact modeling of the emanated seismic wave field and its interaction with
1098 the fault system is crucial. The spatial extend of the Landers fault system leads to dy-
1099 namic triggering effects over large distances, distances large enough to be affected crit-
1100 ically by seismic attenuation.

1101 **4.5 Shallow Slip at the Camp Rock Fault**

1102 It is to-date under debate whether the shallow part of the CRF slipped co-seismically
1103 or if it was triggered by static stress changes shortly after the event [*Sieh, 1996; Kaneda*

1104 *and Rockwell, 2009*]. A lack of aftershock recordings [*Hauksson et al., 1993; Sieh et al.,*
1105 *1993*] as well as the asymmetric right-lateral slip pattern indicate that slip may have been
1106 induced by static stress changes due to the failure of the EF [*Sieh, 1996; Kaneda and*
1107 *Rockwell, 2009*]. Interestingly, slip inversion results based on GPS data [*Wald and Heaton,*
1108 *1994; Hernandez et al., 1999; Gombert et al., 2018*] show higher shallow slip in the north-
1109 ernmost part of the fault system than inversions based on seismic recordings [*Cohee and*
1110 *Beroza, 1994; Cotton and Campillo, 1995*]. However, due to the restriction of most in-
1111 version methods to simplified fault surfaces it is difficult to assign the shallow slip non-
1112 ambiguously to either the EF and CRF.

1113 The here presented dynamic rupture model of the Landers earthquake does not cre-
1114 ate large shallow slip at the northernmost fault segment. The central part of the CRF
1115 is dynamically triggered at a depth of ≈ 8 km. Rupture dies out quickly when it reaches
1116 the surface, without inducing large surface slip. Specifically interesting is the variance
1117 in SSD we infer for the CRF compared to all other fault segments (Fig. 6).

1118 The here assumed regional stress field in conjuncture with the fault geometry at
1119 the CRF inhibits large surface slip. Dynamic rupture experiments varying stress orien-
1120 tations and stress amplitudes reveal that considerably higher surface slip is not possi-
1121 ble to generate while breaking the full fault system and generating reasonable amount
1122 of slip at the the southernmost fault segments. Thus, our dynamic rupture models align
1123 with the hypothesis of statically triggered shallow rupture.

1124 *Kaneda and Rockwell [2009]* investigate the CRF in detail by analyzing tectonic-
1125 geomorphic features along this fault segment. The 1992 rupture at the CRF differs dis-
1126 tinctly from the characteristics of the penultimate and long-term ruptures. In particu-
1127 lar, the vertical motion is almost opposite to previous ruptures. They conclude that the
1128 fault geometry might include a small dipping component at the center of the fault seg-
1129 ment which shows a reverse-slip motion induced by static stress changes. In contrast,
1130 our dynamic rupture model uses a vertical fault geometry for the entire fault system. Fu-
1131 ture work could investigate whether a dipping fault geometry at the center of the CRF
1132 facilitates dynamic rupture activation and propagation at shallow depth or if shallow slip
1133 can only be induced by static stress changes.

1134 5 Conclusions

1135 We present a mechanically viable dynamic rupture scenario of the 1992 Landers
1136 earthquake, which sheds light on the physical mechanisms of rupture transferring between
1137 adjacent fault segments. Our model is characterized by a high degree of realism lead-
1138 ing in turn to a high degree of uniqueness and reproduces a wide range of observations.

1139 The model accounts for high-resolution topography, complex fault system geome-
1140 tries, 3D subsurface structure, viscoelastic attenuation, off-fault plasticity and depth-dependent
1141 cohesion. Earthquake rupture is able to interconnect all geometrically complex segments
1142 of the fault system under the assumption of smoothly varying fault stress and strength
1143 conditions. The simulation reproduces far-field and near-field observations, such as the
1144 total moment rate, final fault slip, seismic waveforms and respective peak ground mo-
1145 tions, as well as off-fault deformation patterns. Our dynamic rupture earthquake sce-
1146 nario allows detailed analysis of the mechanical sustainability of dynamic rupture trans-
1147 fer with respect to the interplay of tectonic stress and local fault strength conditions.

1148 Sustained dynamic rupture of all Landers fault segments poses a strong constraint
1149 on model parametrization. Specifically, the facilitation and timing of rupture transfers
1150 between the principal fault segments determine the amplitude and orientation of initial
1151 fault stresses and friction. Scenarios succeeding in rupture across the entire fault sys-
1152 tem feature very robust slip distribution under variation of nucleation patch sizes and
1153 frictional parameters - however timing of rupture transfers are highly sensitive.

1154 Importantly, the resulting source dynamics depict a variety of rupture transfer mech-
1155 anisms, including dynamic triggering and direct rupture branching and combination of
1156 both; both mechanisms are crucial to drive rupture across the entire fault system. Large
1157 stress changes due to the subsequent, or almost simultaneous, failure of the HVF and
1158 EF enables dynamic triggering of the CRF over distances much larger than previously
1159 suggested.

1160 Our dynamic rupture model reveals that dynamic triggering - often associated with
1161 the observed segmentation of moment release - is not the only feature reducing the mo-
1162 ment release. In particular, rupture deceleration due to complex fault geometry strongly
1163 affects the moment-release rate, thus complicating the inference of rupture transfer mech-
1164 anisms from observations.

1165 In distinction to previous models [*Aochi and Fukuyama, 2002; Aochi et al., 2003*],
1166 we find that a steeply oriented regional stress field (maximum principal stress close to
1167 north) is crucial to allow the northernmost part (CRF) to rupture. Interestingly, large
1168 shallow slip of the CRF is dynamically inhibited in our scenario, supporting the hypoth-
1169 esis of statically triggered shallow rupture at the CRF shortly after the main event [*Sieh,*
1170 *1996; Kaneda and Rockwell, 2009*]. We find that it is impossible to generate consider-
1171 ably higher surface slip by variations in stress orientations and stress amplitudes while
1172 simultaneously breaking the entire fault system and creating reasonable amount of slip
1173 at the southernmost fault segments.

1174 Rupture termination in our model is overall independent of the geometrically pre-
1175 scribed fault endings, with exception of the northernmost section of the HVF. Rupture
1176 is stopped smoothly corresponding to fault orientation towards the principal stress ori-
1177 entation. Our dynamic rupture model therefore provides a consistent explanation for spon-
1178 taneous rupture termination on most of the principal fault segments, although fault struc-
1179 tures in reality continue.

1180 We show that an along-strike variability of the SSD of up to 20% is possible, even
1181 for laterally constant rock cohesion and bulk friction. These variations can be attributed
1182 to different principal stress directions and complex fault geometry. Relatively high SSDs
1183 (up to 50%) are possible for good quality rock without the presence of pre-existing fault-
1184 damage zones if stress drop is high. We observe dramatically increased off-fault defor-
1185 mation in the vicinity of fault bends and intersections, in excellent agreement with re-
1186 cent maps of fault-zone width [*Milliner et al., 2015*]. Good agreement of synthetic wave-
1187 form characteristics and associated peak ground velocities with observations include cap-
1188 turing of the main S-wave pulses, amplitudes, and shaking duration, indicating not only
1189 the quality of dynamic rupture model, but also of the numerical method used.

1190 In contrast to a purely elastic simulation, our viscoelastic-plastic scenario reduces
1191 the mean PGVs in forward direction by up to 35%, while ground motions perpendicu-
1192 lar to the fault are very similar. Rupture transfer and moment rate of the simulation with
1193 plasticity can be partially emulated by an elastic simulation with increased critical slip
1194 distance D_c that leads to slower rupture speeds and longer delays for transferring rup-
1195 ture to adjacent segments. However, the elastic simulation with decreased rupture speed
1196 still overestimates PGVs in forward rupture direction by 11%.

1197 Ground motion variability with respect to fault distance is in general lower for the
1198 simulation with off-fault plasticity, and found to be close to the commonly used value
1199 of 0.56 [e.g., *Boore and Atkinson*, 2008]. However, the simulation accounting for plas-
1200 tic yielding creates higher ground motion variability close to the fault, presumably due
1201 to the heterogeneous distribution of near-fault plastic yielding.

1202 We find that the complex source dynamics of the Landers fault system induce dy-
1203 namic triggering over large distances, which are large enough to be strongly affected by
1204 seismic attenuation. The effect of attenuation on dynamic triggering is pronounced for
1205 models including off-fault plastic deformation. This suggests that our chosen model in-
1206 gredients considerably increase the uniqueness of conditions allowing sustained rupture;

1207 We demonstrate that physics-based modeling of realistically constrained, in-scale
1208 earthquake scenarios may successfully complement and augment earthquake source ob-
1209 servations. An improved understanding of earthquake source physics can be achieved when
1210 combining various representations of natural complexities.

1211 Appendix

1212 A: Cohesive Zone Width

1213 *Wollherr et al.* [2018] find, that the cohesive zone width can vary considerably across
1214 geometrically complex fault systems. The authors suggest that its minimum should pose
1215 the inherent length scale to be resolved instead of an average value. Additionally, a mea-
1216 sured cohesive zone width may vary with underlying (coarse) fault discretization. Only
1217 for sufficiently high resolutions of the fault, one can determine a correct (“numerically
1218 converged”) cohesive zone width. Higher resolutions need to be considered to determine
1219 whether the cohesive zone width reached a stable value (i.e. converged) or if the solu-
1220 tion is still changing with mesh refinement.

1221 To calculate the cohesive zone width, we determine the time of the onset of rup-
1222 ture (RT), as well as the time when shear stresses reach their dynamic value (DS). Us-
1223 ing the rupture speed v_r , the cohesive zone is then defined by the formula $(DS-RT)v_r$.
1224 For our preferred model the minimum cohesive zone width is measured as 155 m located
1225 at the HVF at a depth of 8 km. For a given on-fault resolution of 200 m, the minimum
1226 cohesive zone is then resolved by 0.775 mesh elements (or 4.56 sub-elemental Gaussian
1227 integration points for polynomial degree $p = 4$). Note, that due to the different prin-
1228 cipal stress amplitudes and orientations used in this model, the rupture paths varies from
1229 the scenarios in *Wollherr et al.* [2018] and consequently the cohesive zone width is slightly
1230 smaller than reported therein.

1231 The convergence rates in *Wollherr et al.* [2018] help to determine the potential er-
1232 ror level with respect to a high resolution reference solution given the minimum cohe-
1233 sive zone width resolution and a polynomial degree p . For $p = 4$, the 200 m on-fault res-
1234 olution corresponds to a mean error of 0.16% for peak slip rate time, 4.16% for peak slip
1235 rate, 0.15% for rupture arrival and 0.94% for final slip. These values are sufficiently small
1236 to accurately resolve the source dynamics [*Day et al.*, 2005].

1237 B: Resolved Frequencies

1238 We analyze the distance dependent frequency content of synthetic velocity record-
1239 ings to determine the maximum resolved frequency content of the wave field in our sim-
1240 ulation. Fig. B.1 shows the normalized frequency spectrum of the observed and simu-
1241 lated seismic velocities for a selection of seismic stations. The stations locations are vi-

1242 sualized in Fig. 7. Their full name, R_{JB} -distance, and corresponding V_{s30} -value and can
1243 be found in Table 1.

1244 The highest resolved frequencies are determined by evaluating the maximum fre-
1245 quency for which the synthetic spectra align with the expected ω^{-1} frequency decay. In
1246 particular close to the faults, our simulation reaches very high frequencies without mod-
1247 eling small-scale roughness or pre-stress heterogeneities. The station LUC, which is the
1248 closest station to the fault traces (0.47 R_{JB} -distance), shows frequencies reaching up to
1249 4.0 Hz. The stations YER (24.37 km R_{JB} -distance) in forward direction includes fre-
1250 quencies up to ≈ 3.0 Hz. With increasing distance the resolved frequency content increas-
1251 ingly deviate from an ideal ω^{-1} decay: Stations FRT (64.97 km R_{JB} -distance) and BOR
1252 (87.33 km R_{JB} -distance) reach up to 2.0 Hz and 1 Hz, respectively. In the low veloc-
1253 ity basin of the Salton Sea, station SAL (102.8 km R_{JB} -distance) only resolves a max-
1254 imum frequency of 1.0 Hz. Therefore, to assure consistent frequency ranges of all syn-
1255 thetics, we bandpass filter all stations in Sec. 3.5.2 in between 0.1 and 1.0 Hz.

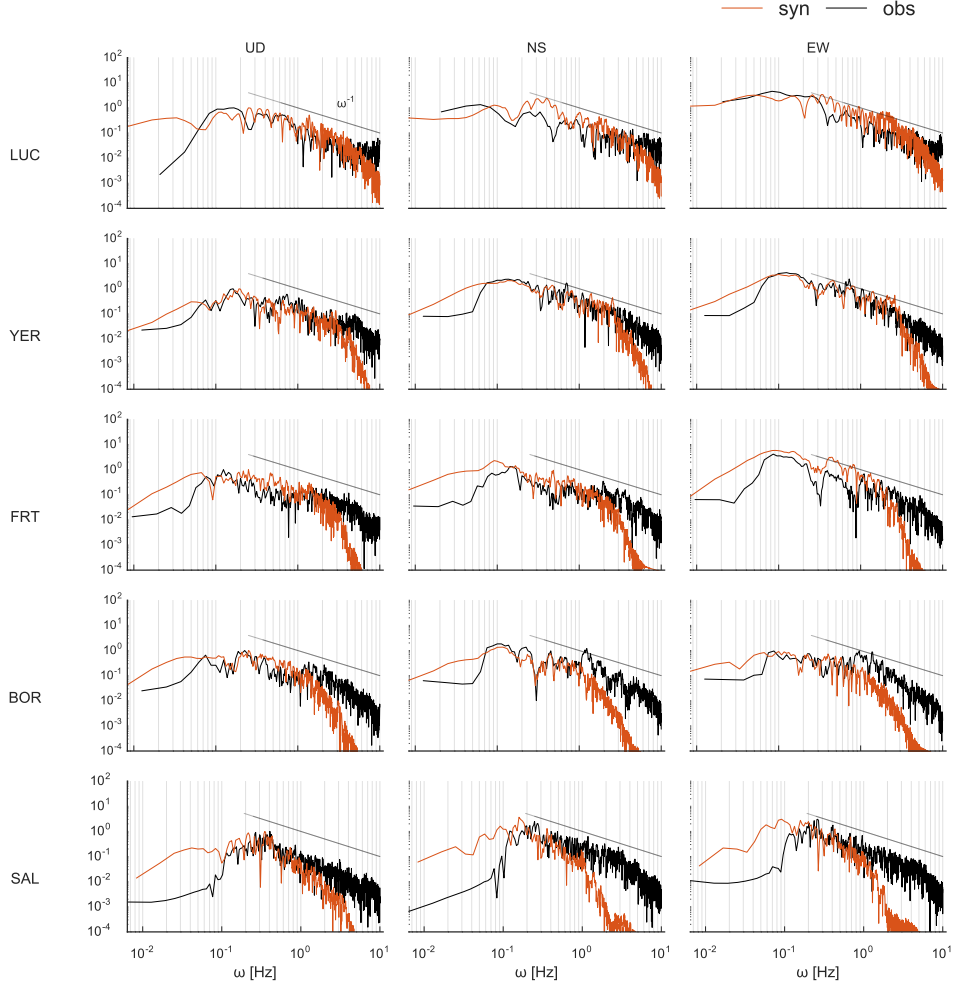


Figure B.1: Normalized frequency spectra for observed (orange) and simulated (black) seismic velocities for a selection of stations listed in Table 1. The stations are ordered by their R_{JB} -distance. The black line indicates the ideally expected frequency decay of ω^{-1} . The frequencies are cut at their respective Nyquist frequency.

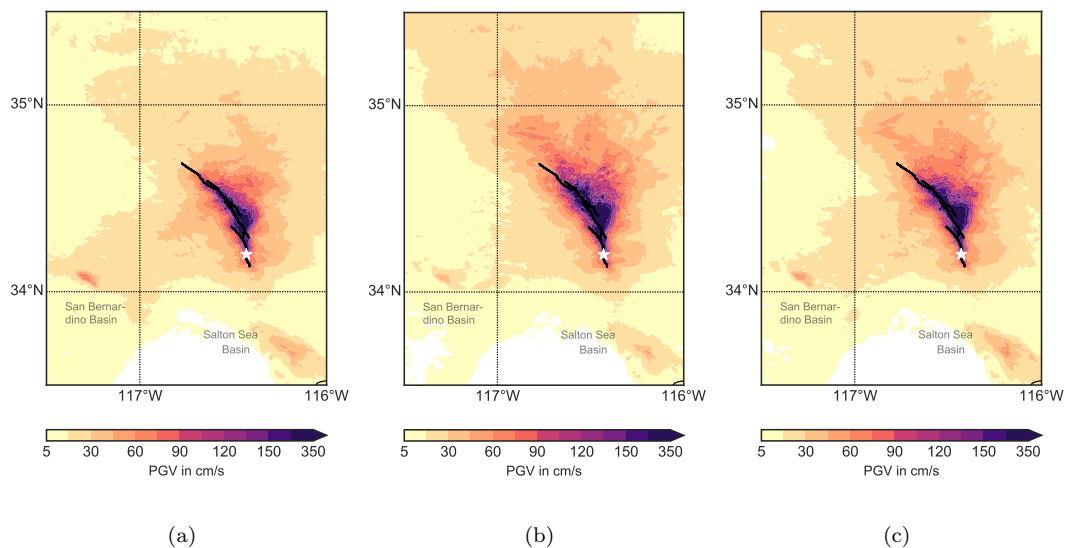


Figure C.1: Simulated GMRotD50 [Boore *et al.*, 2006] PGVs above 5 cm/s for the a) reference simulation with plasticity, b) the corresponding purely elastic simulation and b) for the purely elastic simulation with increased D_c . The white star marks the epicenter of the 1992 event.

1256 C: Peak Ground Motions Maps

1257 We here show a close-up of the PGVs of the three presented simulations in Sec. 4.2:
 1258 the reference simulation with plasticity (Fig. C.1a), the corresponding elastic simulation
 1259 (Fig. C.1b) and the corresponding elastic simulation with increased D_c (Fig. C.1c). Con-
 1260 sistent with the findings for the mean PGVs with respect to the distance or azimuth bins
 1261 in Sec. 4.2, we find that the directivity effect is much more pronounced in the elastic sim-
 1262 ulations. However, an increase of D_c in the elastic simulation drastically reduces the PGVs
 1263 in forward direction while the PGV in the Salton Sea Basin are slightly increased due
 1264 to the slower rupture which results in more backward propagating rupture. Still, ground
 1265 motions in the plastic simulation differ, in particular in the forward direction.

1266 D: Effect of Attenuation on Peak Ground Motions

1267 We discuss in Sec. 4.4 the effect of attenuation on source dynamics, in particular
 1268 on dynamic triggering. Fig. D.1 shows how attenuation affects the the simulated PGVs

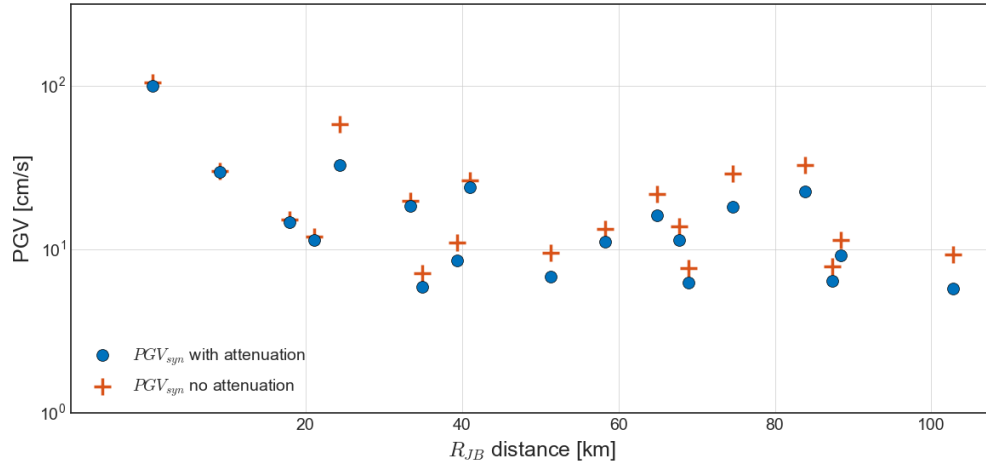


Figure D.1: Simulated PGVs with (blue circles) and without attenuation (orange crosses) in dependence of R_{JB} -distance of the stations given in Table 1.

1269 for the stations listed in Sec. 3.5 and visualized in Fig. 7. While PGVs are almost identical for near fault stations up to 20 km R_{JB} -distance, we observe a clear decrease in PGVs
 1270
 1271 for greater distances due to the attenuation of seismic waves with propagation distance.

1272 **Acknowledgments**

1273 We thank Christopher Milliner for providing the left part of Fig. 11 which is similar to
1274 Fig. 7 in *Milliner et al.* [2015]. All data used are listed in the paper. Simulation results
1275 were obtained using the open-source software package SeisSol, freely available at github.com/SeisSol/SeisSol.
1276 Computing resources were provided by the Leibniz Supercomputing Centre (LRZ, projects
1277 no. pr45fi and pr63qo on SuperMUC). The work presented in this paper was supported
1278 by the German Research Foundation (DFG) (projects no. KA 2281/4-1, GA 2465/2-1,
1279 BA 3529/6-1), by the Bavarian Competence Network for Technical and Scientific High
1280 Performance Computing (KONWIHR), project GeoPF (Geophysics for PetaFlop Com-
1281 puting), by the Volkswagen Foundation (project ASCETE – Advanced Simulation of Cou-
1282 pled Earthquake-Tsunami Events, grant No. 88479), by the European Union’s Horizon
1283 2020 research and innovation program under grant agreement No. 671698 and by King
1284 Abdullah University of Science and Technology (KAUST) in Thuwal, Saudi Arabia, un-
1285 der grant ORS-2016-CRG5-3027-04 and OSR-CRG2017-3389. P. M. Mai is sponsored
1286 through KAUST research fund BAS/1339-01-01.

1287 **References**

- 1288 Abercrombie, R., and J. Mori (1994), Local observations of the onset of a large
1289 earthquake: 28 june 1992 landers, california, *Bulletin of the Seismological Society*
1290 *of America*, 84(3), 725.
- 1291 Ampuero, J.-P., J.-P. Vilotte, and F. Sanchez-Sesma (2002), Nucleation of rupture
1292 under slip dependent friction law: simple models of fault zone, *Journal of Geo-*
1293 *physical Research: Solid Earth*, 107(B12).
- 1294 Ando, R., K. Imanishi, Y. Panayotopoulos, and T. Kobayashi (2017), Dynamic
1295 rupture propagation on geometrically complex fault with along-strike variation
1296 of fault maturity: Insights from the 2014 Northern Nagano earthquake Crustal
1297 Dynamics: Unified Understanding of Geodynamics Processes at Different Time
1298 and Length Scales Yoshihisa Iio, Richard H. Sibson, Toru Takeshita, Takeshi
1299 Sagiya, Bunichiro Shibazaki and Junichi Nakajima, *Earth Planets Space*, 69(1),
1300 doi:10.1186/s40623-017-0715-2.
- 1301 Andrews, D. J. (1999), Test of two methods for faulting on finite-difference calcula-
1302 tions, *Bulletin of the Seismological Society of America*, 89(4), 931–937.

- 1303 Aochi, H., and E. Fukuyama (2002), Three-dimensional nonplanar simulation of the
1304 1992 Landers earthquake, *Journal of Geophysical Research: Solid Earth*, 107(B2),
1305 B22,035, doi:10.1029/2000JB000061.
- 1306 Aochi, H., and R. Madariaga (2003), The 1999 Izmit, Turkey, earthquake: Non-
1307 planar fault structure, dynamic rupture process, and strong ground mo-
1308 tion, *Bulletin of the Seismological Society of America*, 93(3), 1249–1266, doi:
1309 10.1785/0120020167.
- 1310 Aochi, H., R. Madariaga, and E. Fukuyama (2003), Constraint of fault parameters
1311 inferred from nonplanar fault modeling, *Geochemistry, Geophysics and Geosys-*
1312 *tems*, 4(2), 1–16, doi:10.1029/2001GC000207.
- 1313 Barall, M. (2009), A grid-doubling finite-element technique for calculating dynamic
1314 three-dimensional spontaneous rupture on an earthquake fault, *Geophysical Jour-*
1315 *nal International*, 178(2), 845–859, doi:10.1111/j.1365-246X.2009.04190.x.
- 1316 Bhat, H. S., M. Olives, R. Dmowska, and J. R. Rice (2007), Role of fault branches
1317 in earthquake rupture dynamics, *Journal of Geophysical Research: Solid Earth*,
1318 112(B11), B11,309, doi:10.1029/2007JB005027.
- 1319 Bizzarri, A. (2010), How to promote earthquake ruptures: Different nucleation
1320 strategies in a dynamic model with slip-weakening friction, *Bulletin of the Seismo-*
1321 *logical Society of America*, 100(3), 923–940.
- 1322 Bommer, J. J., and N. A. Abrahamson (2006), Why do modern probabilistic
1323 seismic-hazard analyses often lead to increased hazard estimates?, *Bulletin of*
1324 *the Seismological Society of America*, 96(6), 1967–1977.
- 1325 Boore, D. M., and G. M. Atkinson (2008), Ground-motion prediction equations for
1326 the average horizontal component of pga, pgv, and 5%-damped psa at spectral
1327 periods between 0.01 s and 10.0 s, *Earthquake Spectra*, 24(1), 99–138.
- 1328 Boore, D. M., J. Watson-Lamprey, and N. A. Abrahamson (2006), Orientation-
1329 independent measures of ground motion, *Bulletin of the Seismological Society of*
1330 *America*, 96(4A), 1502–1511.
- 1331 Bouchon, M., and M. Campillo (1998), Stress field associated with the rupture of the
1332 1992 Landers, California, earthquake and its implications concerning the fault
1333 strength at the onset of the earthquake, *Journal of Geophysical Research: Solid*
1334 *Earth*, 103(B9), 21,091–21,097.

- 1335 Breuer, A., A. Heinecke, S. Rettenberger, M. Bader, A.-A. Gabriel, and C. Pelties
1336 (2014), Sustained Petascale Performance of Seismic Simulations with SeisSol on
1337 SuperMUC, in *Proceedings of the International Supercomputing Conference*, edited
1338 by J. M. Kunkel, T. Ludwig, and H. W. Meuer, pp. 1–18, Springer International
1339 Publishing, Cham.
- 1340 Breuer, A., A. Heinecke, L. Rannabauer, and M. Bader (2015), High-Order ADER-
1341 DG Minimizes Energy-and Time-to-Solution of SeisSol, in *Proceedings of the In-*
1342 *ternational Conference on High Performance Computing*, edited by J. M. Kunkel
1343 and T. Ludwig, pp. 340–357, Springer International Publishing, Cham.
- 1344 Breuer, A., A. Heinecke, and M. Bader (2016), Petascale local time stepping for
1345 the ADER-DG finite element method, in *2016 IEEE International Parallel and*
1346 *Distributed Processing Symposium*, pp. 854–863, IEEE.
- 1347 Campbell, K. W., and Y. Bozorgnia (1994), Empirical analysis of strong ground
1348 motion from the 1992 landers, california, earthquake, *Bulletin of the Seismological*
1349 *Society of America*, *84*(3), 573.
- 1350 Campillo, M., and R. J. Archuleta (1993), A rupture model for the 28 june 1992
1351 landers, california, earthquake, *Geophysical Research Letters*, *20*(8), 647–650.
- 1352 Candela, T., F. Renard, r. Y. Klinge, K. Mair, J. Schmittbuhl, and E. E. Brodsky
1353 (2012), Roughness of fault surfaces over nine decades of length scales, *Journal of*
1354 *Geophysical Research: Solid Earth*, *117*(B8), doi:10.1029/2011JB009041.
- 1355 Chen, X. (1995), Near-field ground motion from the landers earthquake, Ph.D. the-
1356 sis, California Institute of Technology.
- 1357 Cohee, B. P., and G. C. Beroza (1994), Slip distribution of the 1992 Landers earth-
1358 quake and its implications for earthquake source mechanics, *Bulletin of the Seis-*
1359 *mological Society of America*, *84*(3), 692–712, doi:10.1016/0148-9062(95)94486-9.
- 1360 Cotton, F., and M. Campillo (1995), Frequency domain inversion of strong motions:
1361 Application to the 1992 Landers earthquake, *Journal of Geophysical Research:*
1362 *Solid Earth*, *100*(B3), 3961–3975.
- 1363 Dalguer, L. A., and S. M. Day (2007), Staggered-grid split-node method for sponta-
1364 neous rupture simulation, *Journal of Geophysical Research: Solid Earth*, *112*(2),
1365 1–15, doi:10.1029/2006JB004467.
- 1366 Day, S. M., L. A. Dalguer, N. Lapusta, and Y. Liu (2005), Comparison of fi-
1367 nite difference and boundary integral solutions to three-dimensional sponta-

1368 neous rupture, *Journal of Geophysical Research: Solid Earth*, 110(B12), doi:
1369 10.1029/2005JB003813, b12307.

1370 De la Puente, J., J.-P. Ampuero, and M. Käser (2009), Dynamic rupture model-
1371 ing on unstructured meshes using a discontinuous Galerkin method, *Journal of*
1372 *Geophysical Research: Solid Earth*, 114(B10), b10302.

1373 DeDontney, N., J. R. Rice, and R. Dmowska (2012), Finite Element Modeling of
1374 Branched Ruptures Including Off-Fault Plasticity, *Bulletin of the Seismological*
1375 *Society of America*, 102(2), 541–562, doi:10.1785/0120110134.

1376 Dibblee, T. W. J. (1967), Geologic Map of the Old Woman Springs Quadrangle
1377 San Bernardino County, California, *Tech. rep.*, Department of the Interior United
1378 States Geological Survey.

1379 Dokka, R. K., and C. J. Travis (1990), Late Cenozoic strike-slip faulting in the Mo-
1380 jave Desert, California, *Tectonics*, 9(2), 311–340.

1381 Dreger, D. S. (1994), Investigation of the Rupture Process of the 28 June 1992 Lan-
1382 ders Earthquake Utilizing Terrascope, *Bulletin of the Seismological Society of*
1383 *America*, 84(3), 713–724.

1384 Dumbser, M., and M. Käser (2006), An arbitrary high-order discontinuous
1385 Galerkin method for elastic waves on unstructured meshes II. The three-
1386 dimensional isotropic case, *Geophysical Journal International*, 167(1), 319–336,
1387 doi:10.1111/j.1365-246X.2006.03120.x.

1388 Dunham, E. M., D. Belanger, L. Cong, and J. E. Kozdon (2011a), Earthquake Rup-
1389 tures with Strongly Rate-Weakening Friction and Off-Fault Plasticity, Part 2:
1390 Nonplanar Faults, *Bulletin of the Seismological Society of America*, 101(5), 2308–
1391 2322, doi:10.1785/0120100076.

1392 Dunham, E. M., D. Belanger, L. Cong, and J. E. Kozdon (2011b), Earthquake Rup-
1393 tures with Strongly Rate-Weakening Friction and Off-Fault Plasticity, Part 1: Pla-
1394 nar Faults, *Bulletin of the Seismological Society of America*, 101(5), 2296–2307,
1395 doi:10.1785/0120100075.

1396 Duru, K., and E. M. Dunham (2016), Dynamic earthquake rupture simulations on
1397 nonplanar faults embedded in 3D geometrically complex, heterogeneous elastic
1398 solids, *Journal of Computational Physics*, 305, 185–207.

1399 Ely, G. P., S. M. Day, and J.-B. Minster (2008), A support-operator method for
1400 viscoelastic wave modelling in 3-d heterogeneous media, *Geophysical Journal*

1401 *International*, 172(1), 331–344.

1402 Emerson Paradigm Holding (2018), GoCad: A computer aided design program for
1403 geological applications, <http://www.pdgm.com/products/gocad/>.

1404 Farr, T. G., P. A. Rosen, E. Caro, R. Crippen, R. Duren, S. Hensley, M. Kobrick,
1405 M. Paller, E. Rodriguez, L. Roth, D. Seal, S. Shaffer, J. Shimada, J. Umland,
1406 M. Werner, M. Oskin, D. Burbank, and D. Alsdorf (2007), The shuttle radar
1407 topography mission, *Reviews of Geophysics*, 45(2), doi:10.1029/2005RG000183.

1408 Faulkner, D. R., T. M. Mitchell, E. Jensen, and J. Cembrano (2011), Scal-
1409 ing of fault damage zones with displacement and the implications for fault
1410 growth processes, *Journal of Geophysical Research: Solid Earth*, 116(B5), doi:
1411 10.1029/2010JB007788.

1412 Fialko, Y. (2004a), Probing the mechanical properties of seismically active crust
1413 with space geodesy: Study of the coseismic deformation due to the 1992 Mw 7.3
1414 Landers (southern California) earthquake, *Journal of Geophysical Research: Solid*
1415 *Earth*, 109(B3), B03,307, doi:10.1029/2003JB002756.

1416 Fialko, Y. (2004b), Evidence of fluid-filled upper crust from observations of post-
1417 seismic deformation due to the 1992 Mw 7.3 Landers earthquake, *Journal of*
1418 *Geophysical Research: Solid Earth*, 109(8), 1–17, doi:10.1029/2004JB002985.

1419 Fialko, Y., D. Sandwell, M. Simons, and P. Rosen (2005), Three-dimensional defor-
1420 mation caused by the Bam, Iran, earthquake and the origin of shallow slip deficit,
1421 *Nature*, 435(7040), 295–299, doi:10.1038/nature03425.

1422 Finzi, Y., and S. Langer (2012a), Damage in step-overs may enable large cas-
1423 cading earthquakes, *Geophysical Research Letters*, 39(May), 1–5, doi:10.1029/
1424 2012GL052436.

1425 Finzi, Y., and S. Langer (2012b), Predicting rupture arrests, rupture jumps and cas-
1426 cading earthquakes, *Journal of Geophysical Research: Solid Earth*, 117(12), 1–11,
1427 doi:10.1029/2012JB009544.

1428 Fleming, R., J. Messerich, and K. Cruikshank (1998), Fractures along a portion
1429 of the Emerson fault zone related to the 1992 Landers, California, earthquake:
1430 Evidence for the rotation of the Galway-Lake-Road block, *Geological Society of*
1431 *America, Map and Chart Series*, mCH082.

1432 Fliss, S., H. S. Bhat, R. Dmowska, and J. R. Rice (2005), Fault branching and rup-
1433 ture directivity, *Journal of Geophysical Research: Solid Earth*, 110(B6), B06,312,

1434 doi:10.1029/2004JB003368.

1435 Frey Mueller, J., N. E. King, and P. Segall (1994), The co-seismic slip distribution of
1436 the Landers earthquake, *Bulletin of the Seismological Society of America*, *84*(3),
1437 646–659.

1438 Gabriel, A., J. Ampuero, L. A. Dalguer, and P. M. Mai (2012), The transition of
1439 dynamic rupture styles in elastic media under velocityweakening friction, *Journal*
1440 *of Geophysical Research: Solid Earth*, *117*(B9), doi:10.1029/2012JB009468.

1441 Gabriel, A.-A., J.-P. Ampuero, L. A. Dalguer, and P. M. Mai (2013), Source prop-
1442 erties of dynamic rupture pulses with off-fault plasticity, *Journal of Geophysical*
1443 *Research: Solid Earth*, *118*(8), 4117–4126, doi:10.1002/jgrb.50213.

1444 Galis, M., C. Pelties, J. Kristek, P. Moczo, J.-P. Ampuero, and P. M. Mai (2014),
1445 On the initiation of sustained slip-weakening ruptures by localized stresses, *Geo-*
1446 *physical Journal International*, *200*(2), 890–909, doi:10.1093/gji/ggu436.

1447 Gombert, B., Z. Duputel, R. Jolivet, C. Doubre, L. Rivera, and M. Simons (2018),
1448 Revisiting the 1992 landers earthquake: a bayesian exploration of co-seismic slip
1449 and off-fault damage, *Geophysical Journal International*, *212*(2), 839–852, doi:
1450 10.1093/gji/ggx455.

1451 Graizer, V. M. (2005), Effect of tilt on strong motion data processing, *Soil Dynamics*
1452 *and Earthquake Engineering*, *25*(3), 197–204.

1453 Graves, R. W., B. T. Aagaard, K. W. Hudnut, L. M. Star, J. P. Stewart, and T. H.
1454 Jordan (2008), Broadband simulations for mw 7.8 southern san andreas earth-
1455 quakes: Ground motion sensitivity to rupture speed, *Geophysical Research Letters*,
1456 *35*(22), doi:10.1029/2008GL035750.

1457 Gross, S., and C. Kisslinger (1997), Estimating tectonic stress rate and state with
1458 Landers aftershocks, *Journal of Geophysical Research: Solid Earth*, *102*(B4), 7603,
1459 doi:10.1029/96JB03741.

1460 Harris, R., and S. M. Day (1993), Dynamic of fault interaction: parallel strike-slip
1461 faults, *Journal of Geophysical Research: Solid Earth*, *98*(No. B3), 4461–4472,
1462 doi:10.1029/92JB02272.

1463 Harris, R. A., M. Barall, B. Aagaard, S. Ma, D. Roten, K. Olsen, B. Duan, D. Liu,
1464 B. Luo, K. Bai, J. Ampuero, Y. Kaneko, A. Gabriel, K. Duru, T. Ulrich, S. Woll-
1465 herr, Z. Shi, E. Dunham, S. Bydlon, Z. Zhang, X. Chen, S. N. Somala, C. Pelties,
1466 J. Tago, V. M. CruzAtienza, J. Kozdon, E. Daub, K. Aslam, Y. Kase, K. Withers,

1467 and L. Dalguer (2018), A suite of exercises for verifying dynamic earthquake rup-
1468 ture codes, *Seismological Research Letters*, *89*(3), 1146, doi:10.1785/0220170222.

1469 Hauksson, E. (1994), State of stress from focal mechanisms before and after the 1992
1470 Landers earthquake sequence, *Bulletin of the Seismological Society of America*,
1471 *84*(3), 917–934, doi:10.1016/0148-9062(95)94483-4.

1472 Hauksson, E., L. M. Jones, K. Hutton, and D. Eberhart-Phillips (1993), The 1992
1473 Landers earthquake sequence: Seismological observations, *Journal of Geophysical*
1474 *Research: Solid Earth*, *98*(B11), 19,835–19,858.

1475 Heinecke, A., A. Breuer, S. Rettenberger, M. Bader, A.-A. Gabriel, C. Pelties,
1476 A. Bode, W. Barth, and X.-K. Liao (2014), Petascale High Order Dynamic Rup-
1477 ture Earthquake Simulations on Heterogeneous Supercomputers, in *Proceedings*
1478 *of the International Conference for High Performance Computing, Networking,*
1479 *Storage and Analysis*, pp. 3–15, IEEE, doi:10.1109/SC.2014.6.

1480 Hernandez, B., F. Cotton, and M. Campillo (1999), Contribution of radar interfer-
1481 ometry to a two-step inversion of the kinematic process of the 1992 Landers earth-
1482 quake, *Journal of Geophysical Research: Solid Earth*, *104*(B6), 13,083–13,099.

1483 Hill, R., J. Treiman, J. Given, J. Pechman, J. McMillan, and J. Ebel (1980), Geo-
1484 logic study of the homestead valley earthquake swarm of march 15, 1979, *Califor-*
1485 *nia Geology*, *33*(3), 60–67.

1486 Ida, Y. (1972), Cohesive Force across the Tip of a Longitudinal-Shear Crack and
1487 Griffith’s Specific Surface Energy, *Journal of Geophysical Research: Solid Earth*,
1488 *77*(20), 3796–3805.

1489 Imperatori, W., and P. M. Mai (2015), The role of topography and lateral velocity
1490 heterogeneities on near-source scattering and ground-motion variability, *Geophysi-*
1491 *cal Journal International*, *202*, 2163–2181, doi:10.1093/gji/ggv281.

1492 Kagan, Y. Y., and H. Houston (2005), Relation between mainshock rupture pro-
1493 cess and Omori’s law for aftershock moment release rate, *Geophysical Journal*
1494 *International*, *163*(September), 1039–1048, doi:10.1111/j.1365-246X.2005.02772.x.

1495 Kanamori, H., and L. Rivera (2006), Energy Partitioning During an Earthquake, in
1496 *Earthquakes: Radiated Energy and the Physics of Faulting Geophysical Monograph*
1497 *Series 170*, pp. 3–13, American Geophysical Union.

1498 Kanamori, H., H.-K. Thio, D. Dreger, E. Hauksson, and T. Heaton (1992), Initial in-
1499 vestigation of the landers, california, earthquake of 28 june 1992 using terrascope,

- 1500 *Geophysical Research Letters*, 19(22), 2267–2270.
- 1501 Kaneda, H., and T. K. Rockwell (2009), Triggered and primary surface ruptures
1502 along the camp rock fault, eastern California shear zone, *Bulletin of the Seismo-*
1503 *logical Society of America*, 99(5), 2704–2720, doi:10.1785/0120080310.
- 1504 Käser, M., and M. Dumbser (2006), An Arbitrary High Order Discontinuous
1505 Galerkin Method for Elastic Waves on Unstructured Meshes I: The Two-
1506 Dimensional Isotropic Case with External Source Terms, *Geophysical Journal*
1507 *International*, 166(2), 855–877.
- 1508 Käser, M., V. Herrmann, and J. de la Puente (2008), Quantitative accuracy analysis
1509 of the discontinuous Galerkin method for seismic wave propagation, *Geophysical*
1510 *Journal International*, 173(3), 990–999.
- 1511 Kaven, J. O., and D. D. Pollard (2013), Geometry of crustal faults: Identification
1512 from seismicity and implications for slip and stress transfer models, *Journal of*
1513 *Geophysical Research: Solid Earth*, 118(9), 5058–5070, doi:10.1002/jgrb.50356.
- 1514 Li, Y.-G., K. Aki, D. Adams, A. Hasemi, and W. H. K. Lee (1994a), Seismic
1515 guided waves trapped in the fault zone of the Landers, California, earthquake
1516 of 1992, *Journal of Geophysical Research: Solid Earth*, 99(94), 11,705–11,722,
1517 doi:10.1029/94JB00464.
- 1518 Li, Y.-G., K. Aki, J. E. Vidale, W. H. Lee, and C. J. Marone (1994b), Fine struc-
1519 ture of the landers fault zone: segmentation and the rupture process, *Science*,
1520 265(5170), 367–370.
- 1521 Liu, J., K. Sieh, and E. Hauksson (2003), A structural interpretation of the after-
1522 shock cloud of the 1992 m w 7.3 landers earthquake, *Bulletin of the Seismological*
1523 *Society of America*, 93(3), 1333–1344.
- 1524 Lozos, J. C., D. D. Oglesby, B. Duan, and S. G. Wesnousky (2011), The ef-
1525 fects of double fault bends on rupture propagation: A geometrical parameter
1526 study, *Bulletin of the Seismological Society of America*, 101(1), 385–398, doi:
1527 10.1785/0120100029.
- 1528 Ma, S. (2008), A physical model for widespread near-surface and fault zone damage
1529 induced by earthquakes, *Geochemistry, Geophysics and Geosystems*, 9(11), 1–9,
1530 doi:10.1029/2008GC002231.
- 1531 Madden, E. H., and D. D. Pollard (2012), Integration of surface slip and aftershocks
1532 to constrain the 3D structure of faults involved in the M 7.3 landers earthquake,

1533 Southern California, *Bulletin of the Seismological Society of America*, 102(1),
1534 321–342, doi:10.1785/0120110073.

1535 Madden, E. H., F. Maerten, and D. D. Pollard (2013), Mechanics of nonplanar
1536 faults at extensional steps with application to the 1992 M 7.3 Landers, California,
1537 earthquake, *Journal of Geophysical Research: Solid Earth*, 118(1), 3249–3263,
1538 doi:10.1002/jgrb.50237.

1539 Mai, P. M., D. Schorlemmer, M. Page, J.-P. Ampuero, K. Asano, M. Causse, S. Cus-
1540 todio, W. Fan, G. Festa, M. Galis, et al. (2016), The earthquake-source inversion
1541 validation (siv) project, *Seismological Research Letters*, 87(3), 690–708.

1542 Mai, P. M., M. Galis, K. K. Thingbaijam, J. C. Vyas, and E. M. Dunham (2017),
1543 Accounting for fault roughness in pseudo-dynamic ground-motion simulations,
1544 *Pure and Applied Geophysics*, 174(9), 3419–3450.

1545 Milliner, C. W. D., J. F. Dolan, J. Hollingsworth, S. Leprince, F. Ayoub, and C. G.
1546 Sammis (2015), Quantifying near-field and off-fault deformation patterns of the
1547 1992 M_w 7.3 Landers earthquake, *Geochemistry, Geophysics and Geosystems*, 16,
1548 1577–1598, doi:10.1002/2014GC005693.

1549 Nur, A., H. Ron, and O. Scotti (1989), Kinematics and mechanics of tectonic block
1550 rotations, *Slow Deformation and Transmission of Stress in the Earth*, pp. 31–46.

1551 Oglesby, D. (2008), Rupture Termination and Jump on Parallel Offset Faults,
1552 *Bulletin of the Seismological Society of America*, 98(1), 440–447, doi:10.1785/
1553 0120070163.

1554 Oglesby, D. D., and P. M. Mai (2012), Fault geometry, rupture dynamics and
1555 ground motion from potential earthquakes on the north anatolian fault under
1556 the sea of marmara, *Geophysical Journal International*, 188(3), 1071–1087, doi:
1557 10.1111/j.1365-246X.2011.05289.x.

1558 Olsen, K. B. (1997), Three-Dimensional Dynamic Simulation of the 1992 Landers
1559 Earthquake, *Science*, 278(5339), 834–838, doi:10.1126/science.278.5339.834.

1560 Pelties, C., J. de la Puente, J.-P. Ampuero, G. B. Brietzke, and M. Käser (2012),
1561 Three-dimensional dynamic rupture simulation with a high-order discontinuous
1562 Galerkin method on unstructured tetrahedral meshes, *Journal of Geophysical
1563 Research: Solid Earth*, 117(B2), B02,309, doi:10.1029/2011JB008857.

1564 Pelties, C., A.-A. Gabriel, and J.-P. Ampuero (2014), Verification of an ADER-DG
1565 method for complex dynamic rupture problems, *Geoscientific Model Development*,

1566 7(3), 847–866, doi:10.5194/gmd-7-847-2014,10.5194/gmdd-6-5981-2013.

1567 Peyrat, S., K. B. Olsen, and R. Madariaga (2001), Dynamic modeling of the 1992
1568 Landers earthquake, *Journal of Geophysical Research: Solid Earth*, 106(B11),
1569 26,467–26,482.

1570 Ramirez-Guzman, L., R. W. Graves, K. B. Olsen, O. S. Boyd, C. Cramer,
1571 S. Hartzell, S. Ni, P. Somerville, R. A. Williams, and J. Zhong (2015), Ground-
1572 motion simulations of 1811–1812 new madrid earthquakes, central united states,
1573 *Bulletin of the Seismological Society of America*, 105(4), 1961–1988.

1574 Restrepo-Velez, L. F., and J. J. Bommer (2003), An exploration of the nature of the
1575 scatter in ground-motion prediction equations and the implications for seismic
1576 hazard assessment, *Journal of Earthquake Engineering*, 7(spec01), 171–199.

1577 Rettenberger, S., and M. Bader (2015), Optimizing Large Scale I/O for Petascale
1578 Seismic Simulations on Unstructured Meshes, in *Proceedings of the International
1579 Conference on Cluster Computing*, pp. 314–317, IEEE, Chicago, IL.

1580 Rettenberger, S., O. Meister, M. Bader, and A.-A. Gabriel (2016), ASAGI: A Par-
1581 allel Server for Adaptive Geoinformation, in *Proceedings of the Exascale Appli-
1582 cations and Software Conference 2016*, EASC '16, pp. 2:1–2:9, ACM, New York,
1583 doi:10.1145/2938615.2938618.

1584 Rice, J. R., C. G. Sammis, and R. Parsons (2005), Off-fault secondary failure in-
1585 duced by a dynamic slip pulse, *Bulletin of the Seismological Society of America*,
1586 95(1), 109–134.

1587 Ripperger, J., and P. Mai (2004), Fast computation of static stress changes on 2d
1588 faults from final slip distributions, *Geophysical Research Letters*, 31(18).

1589 Rockwell, T. K., S. Lindvall, M. Herzberg, D. Murbach, T. Dawson, and G. Berger
1590 (2000), Paleoseismology of the Johnson Valley, Kickapoo, and Homestead Valley
1591 faults: Clustering of earthquakes in the eastern California shear zone, *Bulletin of
1592 the Seismological Society of America*, 90(5), 1200–1236.

1593 Roten, D., K. B. Olsen, S. M. Day, Y. Cui, and D. Fäh (2014), Expected seismic
1594 shaking in Los Angeles reduced by San Andreas fault zone plasticity, *Geophysical
1595 Research Letters*, 41(8), 2769–2777, doi:10.1002/2014GL059411.

1596 Roten, D., K. B. Olsen, Y. Cui, and S. M. Day (2015), Quantification of fault zone
1597 plasticity effects with spontaneous rupture simulations, in *Best Practices in
1598 Physics-based Fault Rupture Models for Seismic Hazard Assessment of Nuclear*

1599 *Installations*, Vienna, Austria.

1600 Roten, D., Y. Cui, K. B. Olsen, S. M. Day, K. Withers, W. H. Savran, P. Wang,
1601 and D. Mu (2016), High-frequency nonlinear earthquake simulations on petascale
1602 heterogeneous supercomputers, in *Proceedings of the International Conference for*
1603 *High Performance Computing, Networking, Storage and Analysis*, pp. 82:1–82:12,
1604 IEEE.

1605 Roten, D., K. B. Olsen, and S. M. Day (2017), Off-fault Deformations and Shal-
1606 low Slip Deficit from Dynamic Rupture Simulations with Fault Zone Plastic-
1607 ity, *Geophysical Research Letters*, pp. n/a–n/a, doi:10.1002/2017GL074323,
1608 2017GL074323.

1609 Sauber, J., W. Thatcher, and S. C. Solomon (1986), Geodetic measurement of defor-
1610 mation in the central mojave desert, california, *Journal of Geophysical Research:*
1611 *Solid Earth*, 91(B12), 12,683–12,693.

1612 Shaw, J. H., A. Plesch, C. Tape, M. P. Suess, T. H. Jordan, G. Ely, E. Hauksson,
1613 J. Tromp, T. Tanimoto, R. Graves, K. Olsen, C. Nicholson, P. J. Maechling,
1614 C. Rivero, P. Lovely, C. M. Brankman, and J. Munster (2015), Unified Structural
1615 Representation of the southern California crust and upper mantle, *Earth and*
1616 *Planetary Science Letter*, 415, 1–15, doi:10.1016/j.epsl.2015.01.016.

1617 Shi, Z., and S. M. Day (2013), Rupture dynamics and ground motion from 3d rough-
1618 fault simulations, *Journal of Geophysical Research: Solid Earth*, 118(3), 1122–
1619 1141, doi:10.1002/jgrb.50094.

1620 Sieh, K. (1996), The repetition of large-earthquake ruptures., *Proceedings of the Na-*
1621 *tional Academy of Sciences: "Earthquake Prediction: The Scientific Challenge"*,
1622 93(9), 3764–3771, doi:10.1073/pnas.93.9.3764.

1623 Sieh, K., L. Jones, E. Hauksson, K. Hudnut, D. Eberhart-Phillips, T. Heaton,
1624 S. Hough, K. Hutton, H. Kanamori, A. Lilje, et al. (1993), Near-field investiga-
1625 tions of the landers earthquake sequence, april to july 1992, *Science*, 260(5105),
1626 171–176.

1627 Simmetrix Inc. (2017), SimModeler: Simulation Modeling Suite 11.0 Documentation,
1628 *Tech. rep.*, www.simmetrix.org.

1629 Sleep, N. H. (2012), Site resonance from strong ground motions at lucerne, califor-
1630 nia, during the 1992 landers mainshock, *Bulletin of the Seismological Society of*
1631 *America*, 102(4), 1505, doi:10.1785/0120110267.

1632 Sowers, J. M., J. R. Unruh, W. R. Lettis, and T. D. Rubin (1994), Relationship
1633 of the Kickapoo Fault to the Johnson Valley and Homestead Valley Faults, San
1634 Bernardino County, California, *Bulletin of the Seismological Society of America*,
1635 *84*(3), 528–536.

1636 Spotila, J. A., and K. Sieh (1995), Geological investigation of a slip gap in the sur-
1637 ficial ruptures of the 1992 Landers earthquake, southern California, *Journal of*
1638 *Geophysical Research: Solid Earth*, *100*(94), 543–559.

1639 Spudich, P., and B. S. Chiou (2008), Directivity in nga earthquake ground motions:
1640 Analysis using isochrone theory, *Earthquake Spectra*, *24*(1), 279–298.

1641 Strasser, F. O., N. A. Abrahamson, and J. J. Bommer (2009), Sigma: Issues, in-
1642 sights, and challenges, *Seismological Research Letters*, *80*(1), 40–56.

1643 Suppe, J. (1985), *Principles of structural geology*, Prentice Hall.

1644 Tago, J., V. M. Cruz-Atienza, J. Virieux, V. Etienne, and F. J. Sánchez-Sesma
1645 (2012), A 3D hp-adaptive discontinuous Galerkin method for modeling earth-
1646 quake dynamics, *Journal of Geophysical Research: Solid Earth*, *117*(3), 1–21,
1647 doi:10.1029/2012JB009313.

1648 Unruh, J. R., W. R. Lettis, and J. M. Sowers (1994), Kinematic Interpretation of
1649 the 1992 Landers Earthquake, *Bulletin of the Seismological Society of America*,
1650 *84*(3), 537–546.

1651 Uphoff, C., and M. Bader (2016), Generating high performance matrix kernels for
1652 earthquake simulations with viscoelastic attenuation, in *Proceedings of the 2016*
1653 *International Conference on High Performance Computing and Simulation*, edited
1654 by W. W. Smari, pp. 908–916, IEEE.

1655 Uphoff, C., S. Rettenberger, M. Bader, E. H. Madden, T. Ulrich, S. Wollherr, and
1656 A.-A. Gabriel (2017), Extreme scale multi-physics simulations of the tsunamigenic
1657 2004 sumatra megathrust earthquake, in *Proceedings of the International Confer-*
1658 *ence for High Performance Computing, Networking, Storage and Analysis*, SC '17,
1659 pp. 21:1–21:16, ACM, New York, NY, USA, doi:10.1145/3126908.3126948.

1660 Vallée, M., and V. Douet (2016), A new database of source time functions (STFs)
1661 extracted from the SCARDEC method, *Physics of the Earth and Planetary Interi-*
1662 *ors*, *257*, 149–157.

1663 Vyas, J. C., P. M. Mai, and M. Galis (2016), Distance and azimuthal dependence
1664 of ground-motion variability for unilateral strike-slip ruptures, *Bulletin of the*

1665 *Seismological Society of America*, 106(4), 1584–1599, doi:10.1785/0120150298.

1666 Wald, D. J., and T. H. Heaton (1994), Spatial and Temporal Distribution of Slip for
1667 the 1992 Landers, California, Earthquake, *Bulletin of the Seismological Society of*
1668 *America*, 84(3), 668–691.

1669 Wenk, S., C. Pelties, H. Igel, and M. Käser (2013), Regional wave propagation using
1670 the discontinuous Galerkin method, *Journal of Geophysical Research: Solid Earth*,
1671 4(1), 43–57, doi:10.5194/se-4-43-2013.

1672 Wesnousky, S. G. (2006), Predicting the endpoints of earthquake ruptures, *Nature*,
1673 444(7117), 358–360.

1674 Wollherr, S., A.-A. Gabriel, and C. Uphoff (2018), Implementation, verification and
1675 application of off-fault plasticity in three-dimensional dynamic rupture simula-
1676 tions on complex fault geometries using a modal Discontinuous Galerkin method,
1677 *Geophysical Journal International*.

1678 Xu, X., X. Tong, D. T. Sandwell, C. W. D. Milliner, J. F. Dolan, J. Hollingsworth,
1679 S. Leprince, and F. Ayoub (2016), Refining the shallow slip deficit, *Geophysical*
1680 *Journal International*, 204(3), 1867–1886, doi:10.1093/gji/ggv563.

1681 Zeng, Y., and J. G. Anderson (2000), *Evaluation of numerical procedures for sim-*
1682 *ulating near-fault long-period ground motions using Zeng method*, Pacific Earth-
1683 quake Engineering Research Center.

1684 Zielke, O., M. Galis, and P. M. Mai (2017), Fault roughness and strength hetero-
1685 geneity control earthquake size and stress drop, *Geophysical Research Letters*,
1686 44(2), 777–783, doi:10.1002/2016GL071700.